



UNIVERSITAT POLITÈCNICA DE CATALUNYA
BARCELONATECH

Escola Tècnica Superior d'Enginyeria
de Telecomunicació de Barcelona



Treball Final del Grau en Enginyeria Física

Ultrasound-based flow measurement system for water flux in a perfusion phantom

Degree Thesis carried out at the Graz University of Technology and submitted
to the Faculty of the Escola Tècnica d'Enginyeria de Telecomunicació de
Barcelona

Universitat Politècnica de Catalunya

by

Pau Sindreu Cladera

In partial fulfillment of the requirements for the degree in
Enginyeria Física

Advisors: Hermann Scharfetter, Jaime Oscar Casas Piedrafita
Graz, Austria, June 2023



Acknowledgements

First of all, I want to thank my thesis director Hermann Scharfetter for the countless hours he has spent helping and advising me on this thesis. I am truly grateful for all his advice, patience and rigour. The amount of things I have learnt in these 5 months wouldn't be the same if it weren't for his knowledge and experience. I also want to thank my co-director Oscar Casas for all the help he has provided from the distance. Moreover, I also appreciate the support, company and ideas of from the members of the Institute of Biomedical Imaging from TU Graz, and for all the time we have spent together. Herzlichen dank!

També voldria agrair als meus pares, Josep i Tònia, i la meva germana Ona pel suport moral, les idees i les solucions que m'han donat. Els consells de bricolatge del meu pare han estat increïblement útils sempre que ho he necessitat.

I per acabar, als meus amics del grau d'Enginyeria Física per haver passat amb ells aquests magnífics quatre anys, i per haver estat al meu costat sempre que ho he necessitat. Sense ells, la carrera hauria estat molt més dura.

Contents

List of Figures	iv
List of Tables	v
1 Introduction	1
1.1 Motivation and problem statement	1
1.2 Current technologies and research	1
1.3 Objectives	2
2 Theoretical background	4
2.1 Ultrasound transducers and propagation	4
2.1.1 Transducers	4
2.1.2 Acoustic impedance	4
2.2 Ultrasonic sensing applications	6
2.2.1 Distance measurement	6
2.2.2 Velocity measurement	6
2.2.2.1 Time of Flight	6
2.2.2.2 Doppler Effect	9
2.3 Signal processing techniques	9
2.3.1 In-phase and Quadrature demodulation	9
2.3.2 Sinusoidal phase estimation	10
3 Developement of the measurement system	11
3.1 Measurement methods	11
3.1.1 Time of Flight	11
3.1.2 Doppler Effect	11
3.2 Instrumentation	12
3.2.1 FPGA	12
3.2.1.1 Pulse generation	13
3.2.1.2 Data acquisition and further processing	13
3.2.2 Signal driver	14
3.2.2.1 Differential line driver	14
3.2.2.2 RF transformer	14
3.2.3 Low Noise Amplifier	15
3.2.4 Switch board	16
3.3 Noise analysis	18
4 Software development	21
4.1 Server application	21
4.2 Client application	22
4.3 Program flow	23
4.4 Options and limitations	23
5 Measurements, results and discussion	25
5.1 Phase estimation algorithm verification	25

5.2	Interference reduction	26
5.3	Velocity measurements in a 24 mm PVC tube	27
5.3.1	Measurements with phase shift	27
5.3.2	Measurements with Doppler Effect	29
5.4	Velocity measurements in phantom: circular tube	31
5.5	Velocity measurements in phantom: rectangular cross-section	33
5.5.1	Superposition of ultrasonic waves	35
5.5.1.1	Adaptive filter	42
5.5.1.2	Acoustic beam collimator	43
5.6	Velocity measurements in the tube inside the phantom with collimator . .	44
5.7	Velocity measurements in the tube inside the phantom with collimator and clamping structure	45
6	Conclusions and future work	47
	Appendices	52
A	Appendix: Manual	53
A.1	Hardware	53
A.2	Software	53
B	Appendix: Switch board	55
B.1	Schematic	55
B.2	PCB layout	56

List of Figures

1	Perfusion phantom	1
2	Different placement of transducers depending on the application	6
3	Block diagram of the different components of the flow-meter	12
4	FPGA block diagram [11]	13
5	<i>Balun</i> schematic	15
6	Schematic of the Low Noise Amplifier made with Eagle (Autodesk, Inc, USA)	16
7	Pin configuration of MAX333A Analog Multiplexer	17
8	Schematic of 4 channel analog switch PCB	18
9	Op Amp noise analysis circuit [17]	19
10	Registers in the FPGA	22
11	Data structure after reading from buffer	22
12	Graphical User Interface	23
13	Flow diagram of the software	24
14	Phase of received pulses with two different coaxial cables	26
15	Cross-talk whilst using neighboring twisted pairs in the same cable (blue) and twisted pairs in different cables (isolated)	27
16	Centrifugal Pump used for all the measurements in this project.	28
17	Support structure printed to hold the transducers attached to the tube.	29
18	Phase of received pulses with increasing velocities from 0 to 8.8 l/min and switching every 20 pulses.	30
19	Phase change of received pulse during 20 minutes.	31
20	Set-up of transducers to detect reflections.	31
21	Fourier transform of the received signal for flows of 8.8, 8.1, 7, 5.5, 4 and 3 l/min, from left to right and top to bottom, respectively.	32
22	Comparison between real flow values and estimated.	33
23	Transducers placed on top of the glass above the tube.	33
24	Phase difference of the upstream and downstream pulses with the transducers placed on the tube when increasing the flow at the pump by 0.5 l/min.	34
25	Image of the perfusion phantom taken with the MRI scanner using Phase Contrast MRI. [22]	34
26	Phase difference between upstream and downstream pulses when increasing flow by 0.5 l/min repeatedly.	35
27	Phase of downstream pulse with the transducers set in direct transmission (left) and phase difference between upstream and downstream (right).	36
28	Some of the possible reflections inside the phantom.	37
29	Description and definition of angles in the case in which there are no reflections ($n = 0$) (top) and when there are 2 reflections ($n = 1$) (bottom)	38
30	Output angles from the TX transducer to reach the RX transducer with $2 \cdot n$ reflections (left axis), attenuation due to reflections and longer path (right axis)	39
31	Simulated absolute phase of upstream and downstream pulses (left) and their difference (right).	40

32	Simulated phases in the two cases: height change but no reflections considered (left), reflections considered ($N = 5$) but no change in height (right). .	41
33	Block diagram of an adaptive filter.	42
34	Blueprint of the collimator	43
35	5° collimator built.	44
36	Absolute phase of the pulses in both directions when a 3.5° collimator is used(left) and their difference (right).	44
37	Difference in concavity in 8.8 l/min (top) and 0 l/min (bottom).	45
38	Clamping structure to prevent the movement of the acrylic glass.	46
39	Measurements after adding clamping device to prevent movement. Absolute phases (left) and differential phases (right).	47
40	Measures taken with increasing the flux read at the pump every 5 seconds and changing with steps of 0.5 l/min.	48
41	Comparison of velocity values after calibration with MRI.	49
42	From Red Pitaya Schematics [26]	53
43	Pin description of the hardware	54
44	Schematic of analog switch	55
45	PCB layout of analog switch	56

Listings

List of Tables

1	Properties of different relevant materials [9]	5
2	Reflectance and Transmission coefficients for the different media changes in a typical ultrasonic water application	5

Abstract

In this project, local velocities of water inside a perfusion phantom have been measured by sending Ultrasound pulses and measuring the time it takes them to travel upstream and downstream. The difference in their propagation time, the Δ Time of Flight, theoretically follows a linear relationship with the flow through the pipe.

The measurement system has been built using a Red Pitaya Stemlab 125-14 board, which is used to generate the pulses of 200 ms long and frequency 975 kHz, read the received signal and process it digitally in the FPGA. The pulses from the DAC are amplified with a MAX4147 differential line driver and then emitted acoustically with a *US-0014 Audiowell* transducer with 5V peak to peak. The transmitted signal is received with an identical transducer and amplified via a Differential Amplifier with gain 38. It is then sampled with a 14 bit ADC. The software controlling the Red Pitaya has a Server-Client architecture with a PC sending the orders and receiving and processing the data. The Δ ToF is calculated by means of a phase estimation algorithm that uses the In Phase and Quadrature components of the received signals.

The linearity between the measured phase difference and reference flow has been found, in agreement with the theoretical estimation using a rectangular cross section and a 1D laminar flow in the vertical direction. A variance of less than 0.05 cm/s has been found for velocities in the range of 0 to 1 cm/s, which are the values possible with the pump.

Features and limitations of the method have been investigated and characterized. Due to non-idealities of the used flow phantom and the lack of a reference flow-meter the measurement results must still be interpreted with caution. However, a working prototype has been established successfully.

1 Introduction

1.1 Motivation and problem statement

In the field of biomedical engineering and research, phantoms are testing devices with the purpose of substituting real tissue during the developing stages of design and test of medical devices. In the magnetic resonance imaging (MRI) context, phantoms are common in research for evaluating the performance of the device, as well as to perform studies of tissue behavior without the need of real persons. It is the case of phantoms to study flow phenomena in veins and arteries. In the Institute for Biomedical Imaging of the Graz University of Technology (Austria), where this thesis has been carried out, currently there is a project for developing new accurate and fast MRI sequences to measure local fluid with a scanner. For some time, researchers in this group have been developing and testing different phantoms, pipes and pumps. For this reason, a flow meter was needed to measure in a non-intrusive way the velocity inside the different set-ups.

In his Master's degree and PhD research, Ansgar Adler built a perfusion phantom [1], shown in Figure 1. Water flows from left to right; as soon as it enters the box, it goes through a sponge to homogenize the flow along all the cross-section, and then through the straws to generate a laminar flow. At the last part of the phantom, there is a circular PVC pipe. The main goal of the research is to be able to measure the flow inside this pipe.

There are many different techniques to measure the velocity of a fluid, including Coriolis [2], differential pressure [3], vortex [4], magnetic [5], ultrasonic [6] and turbine [7]. From this list, the most non-intrusive type is ultrasound.



Figure 1: Perfusion phantom

1.2 Current technologies and research

Nowadays, water flow measurement is widely used in industry, automation and research. There are many commercially available devices which can perform this task. However, the vast majority of these solutions include intrusive elements and do not allow for adaptation to different applications. Flow meters can be categorized in the following way [8]:

- Fully mechanical: provide a simple and low cost sensors, but have a limited accuracy, narrow measurement range and require high maintenance.

- Electromechanical: can provide real-time information but require extra protection
- Fully electronic: can provide high-accuracy, real-time information and can be non-intrusive, but require waterproof protection and the design can be more complex.

Most flow meters used in industry are included in the first two categories, which cannot function for the purpose of this project, since the main requirement is to be non-intrusive to not disturb the flow. The chosen method is ultrasound. Ultrasonic waves can travel through water or any medium in a non-intrusive manner and can provide information on several properties.

To send and receive the ultrasonic signal, an ultrasonic transducer is needed. It is a device able to generate and sense ultrasonic waves. It converts an electric signal to an ultrasonic signal and vice versa, depending on its use. These elements are widely used in medicine for non-invasive imaging.

For flow measurement, the two most used methods are Doppler Effect (DE) and Δ Time of Flight (Δ ToF). Both require one transducer to act as emitter of the ultrasonic signal and another one as receiver. However, the main difference is that in Doppler Shift, the interest is in the shift in frequency of the received signal with respect to the emitted signal, and the Δ ToF is centered on the time difference between the up-stream signal and the down-stream signal. In the theoretical section, both methods will be studied, as well as their feasibility to be applied in our conditions.

1.3 Objectives

In the used phantom, there is a need of measuring the liquid flow through one of its pipes. Thus, it is important to be able to achieve with the following requisites:

- Avoiding disturbing the flow profile of the fluid
- Measuring speeds from 0.2 cm/s to 200 cm/s
- Avoiding damages or modifying as little as possible the phantom
- Avoiding disturbing the applied magnetic field to not interfere the imaging
- Be non-magnetic for safety reasons

The design must contain different systems with the following functions:

1. Instrumentation

- (a) Pulse generator and oscilloscope
- (b) Driving circuit to provide enough power to the emitter transducer
- (c) Amplifier circuit for signal conditioning
- (d) Switch to change the emitting and receiving transducer (in case the Δ ToF method is used)
- (e) Coupling system between phantom and transducer

2. Software: Client-server architecture to send the pulses and receive the data correctly
3. Digital algorithm to quantify the local flow velocity

The main goal of this project is to design a measurement system able to determine the fluid flow through the pipe inside the phantom fulfilling the previous requirements. This system must be able to send a signal capable of going through the media and be received with enough power by the receiver. Afterwards, the received signal must be processed and analyzed to give, as a result, the flux of the liquid.

The first step of the project is to design a system for sending and receiving ultrasonic pulses with the transducers, including the software to run the excitation and acquisition system. In parallel, the theory behind both methods should be studied, and the requirements of the pulse generation and acquisition systems should be determined in order to obtain enough resolution with the flow measurements.

Once the acquisition is valid and the requisites for the pulses are clear, the next goal should be to build a first water circuit able to attach transducers on a tube with flowing water and try to make some measurements. This should allow to chartacterize the obtained signals and develop methods for optimizing the system.

After that, a final prototype for making measures should be built, with a tube similar to the phantom but in a smaller dimension, easier to handle. The idea is to couple the transducer to a pipe with a 3-D printed design, and observe the acoustic properties of the pipe. If the measurements show satisfactory results, we should be able to use the perfusion phantom to make the final measurements.

2 Theoretical background

2.1 Ultrasound transducers and propagation

2.1.1 Transducers

An ultrasonic transducer is a sensing device based on a piezoelectric material. These materials have the particularity of being able to generate an electric field due to a stress applied on them. Alternatively, they can also be deformed based on the electric field applied on them. These are called piezoelectric effect and inverse piezoelectric effect, respectively.

When a voltage is applied between the two terminals, an electric field will be generated, producing an induced polarization which in turn will create a stress on the crystal. If this voltage is increased and decreased rapidly, a vibration in the crystal appears. This can produce a vibration in the medium surrounding the crystal in the direction of the strain, which is known as a sound wave. The frequency of oscillation of the electrical signal can determine the frequency of the sound wave. Each piezoelectric crystal has a different resonant frequency. Transducers with a low resonant frequency start around 30 kHz. The resonant frequency is the one in which electrical impedance of the piezoelectric element has a sharp extremum. It is minimum in series resonance, but there also exists a maximum in the frequency of parallel resonance, both of which provide better sensitivity and efficiency.

The behaviour of a transducer is given by the piezoelectric properties of the crystal it is made of, which can be barium titanate, lead zirconate titanate (PZT) and Rochelle salt. For this particular application, transducers have a disk shape, and the wires are connected to the two sides. Both direct and inverse piezoelectric effects are used, the former for sensing the vibration and the latter to generate one.

2.1.2 Acoustic impedance

As any other wave, when an ultrasonic wave encounters a different medium, part of the energy is reflected, part is absorbed and part is transmitted. When an elastic medium vibrates, the deformation propagates through the medium. This propagation can be characterized by three quantities: frequency, amplitude and atomic instantaneous velocity. For air, propagation velocity is around 330 m/s; for water, 1480 m/s; fat, 1450 m/s; most metals, around 6000 m/s.

When there is a perturbation, the pressure at a particular point oscillates around the average value before the perturbation. Acoustic pressure p is defined as the difference between instantaneous pressure and average pressure. It can be shown that when the medium is loss-less and p and v are real quantities, acoustic impedance is $Z = \rho \cdot c$, and is characteristic of every medium. The following table shows propagation velocity and acoustic impedance in different media:

Intensity is defined as the power of the wave per unit area: $I = \frac{p^2}{Z}$, and if the medium of

Medium	Speed of Ultrasound (m/s)	Acoustic impedance ($kg/(m^2s)$)
Air	330	429
Water	1500	$1.5 \cdot 10^6$
Blood	1570	$1.66 \cdot 10^6$
Fat	1450	$1.34 \cdot 10^6$
Barium titanate	5500	$30.8 \cdot 10^6$
Aluminium	6420	$16.65 \cdot 10^6$
PVC	1380	$3.27 \cdot 10^6$
Polypropylene	2740	$2.40 \cdot 10^6$
Acrylic glass	2750	$3.26 \cdot 10^6$

Table 1: Properties of different relevant materials [9]

propagation is homogeneous, its magnitude decreases exponentially with distance x .

$$I = I_0 \cdot e^{-kfx} \quad (1)$$

, where k is the attenuation coefficient, and f is the ultrasonic signal frequency.

When the ultrasonic wave encounters a change of media, that is, the acoustic impedance of the media changes, a part of the energy is transmitted and a part is reflected.

Reflectance and Transmission coefficients can be defined as the ratio between reflected and incident intensity, and transmitted and incident intensity, respectively, for normal incidence.

$$R = \frac{I_r}{I_i} = \left(\frac{Z_1 - Z_2}{Z_1 + Z_2} \right)^2 \quad (2)$$

$$T = \frac{I_t}{I_i} = \frac{4 \cdot Z_1 \cdot Z_2}{(Z_1 + Z_2)^2} \quad (3)$$

In an typical ultrasonic application in water, where the vibrations begin at the piezoelectric material (BTO), transmit to the Aluminium, then to water, and are received with another identical transducer, the transmission coefficient is roughly 7%.

If we include going through a Polypropylene pipe, reflecting at its other wall, and transmitting back and then sensing it at the outside, the received power is significantly lower. Thus, a very strong signal has to be sent, and then amplified with a very large gain.

Media change	R	T
BTO-Al	0.0889	0.9111
Al-H2O	0.6961	0.3033

Table 2: Reflectance and Transmission coefficients for the different media changes in a typical ultrasonic water application

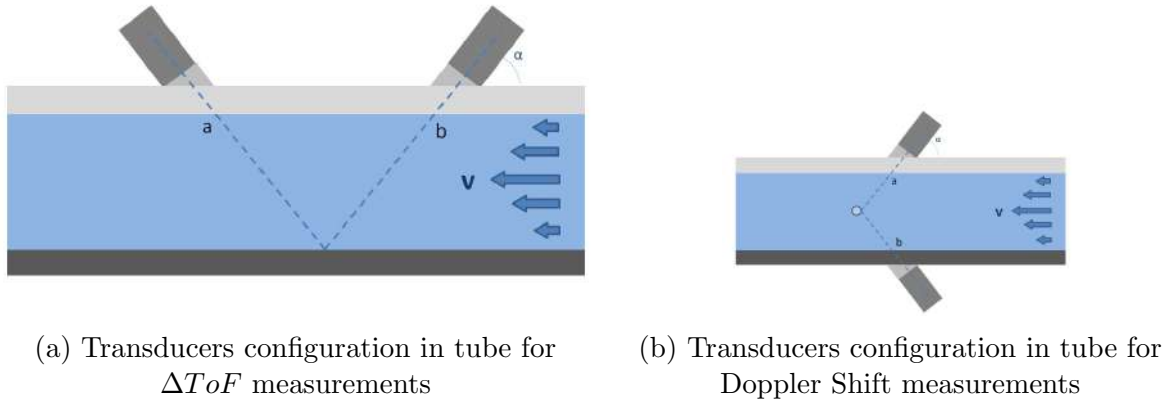


Figure 2: Different placement of transducers depending on the application

2.2 Ultrasonic sensing applications

2.2.1 Distance measurement

The most basic measurement that can be performed with a pair of ultrasonic transducers is distance measurements in water. If the velocity of sound in the medium is known, the calculation of the distance to a particular object is trivial. The two transducers are placed next to each other pointing at the object, and one transducer sends a sinusoidal pulse and the other one receives it. By measuring the time it takes the wave to travel to the object and return, one can obtain the distance: $d = \frac{1}{2} \cdot \frac{\Delta t}{c}$. This method is widely used in research and industry and is not the interest for the current project.

2.2.2 Velocity measurement

The measurement of interest for this project is velocity. The two most frequently used methods are Time of Flight and Doppler Effect methods. Both rely on the propagation of an ultrasonic wave through a fluid, but are based on different principles.

2.2.2.1 Time of Flight This method relies on the time difference of a wave propagating upstream or downstream. For a wave propagating from point a to b, the time it takes to go from one point to another is given by the distance, the velocity of the wave, and the velocity of the fluid. We suppose the configuration of figure 2a is used, where the beam reflects at the bottom of the pipe and crosses the flow again:

$$t_{UPS} = \frac{L}{c - v \cos \alpha} \quad (4)$$

$$t_{DNS} = \frac{L}{c + v \cos \alpha} \quad (5)$$

However, this is only true for the case of uniform velocity profiles. In reality, $v = v(l)$, l being the distance from the transmitter, measured along the propagation direction, and

we need to consider the profile. Equations 6 and 7 are only valid in a small distance dL , and these can be rewritten as:

$$dt_{UPS} = \frac{dL}{c - v \cos \alpha} \quad (6)$$

$$dt_{DNS} = \frac{dL}{c + v \cos \alpha} \quad (7)$$

The main assumption is that we assume that the reflection is only from a single point at the bottom of the pipe. Firstly we will consider the case of a circular cross-section of radius R . Subsequently, we can integrate along the path of the wave. The angle between the beam and the flow is α and we can use the relation $L = \frac{4R}{\sin \alpha}$ to change the integrating variable to the radial direction. The factor 4 at the front comes from the sum of both incidence and reflection path.

$$t_{UPS} = \int_0^L \frac{dl}{c - v \cos \alpha} = \int_0^R \frac{dr}{c - v \cos \alpha} \cdot \frac{4}{\sin \alpha} \quad (8)$$

We can use the fact that c is at least 3 orders of magnitude larger than v , and use the Taylor series of $\frac{1}{1-x}$ when x tends to 0,

$$f(x) = \frac{1}{1 \pm x} \approx 1 \mp x \quad (9)$$

Additionally we can introduce a dimensionless radius $s = \frac{r}{R}$ and the equation is:

$$t_{UPS} = \frac{4R}{c \sin \alpha} \int_0^1 \left(1 + \frac{v}{c} \cos \alpha\right) ds \quad (10)$$

The time difference will be:

$$\begin{aligned} \Delta ToF &= t_{UPS} - t_{DNS} = \frac{4R}{c \sin \alpha} \int_0^1 \left(1 + \frac{v}{c} \cos \alpha\right) ds - \frac{4R}{c \sin \alpha} \int_0^1 \left(1 - \frac{v}{c} \cos \alpha\right) ds \\ &= \frac{8R}{c \sin \alpha} \int_0^1 \frac{v}{c} \cos \alpha ds = \frac{8R \cos \alpha}{c^2 \sin \alpha} \int_0^1 v ds \end{aligned} \quad (11)$$

Moreover, equation 11 shows that the time difference is proportional to the flux, without having to take into account the type of velocity profile. If we consider a laminar flow, which is the one we expect to find inside the phantom, the velocity profile will be

$$v = v_m \left(1 - \left(\frac{r}{R}\right)^2\right) = v_m (1 - s^2) \quad (12)$$

and the final ΔToF as a function of velocity is

$$\Delta ToF = \frac{8R \cos \alpha v_m}{c^2 \sin \alpha} \int_0^1 (1 - s^2) ds = \frac{16R \cot \alpha}{3c^2} v_m \quad (13)$$

If take a quick look at the result, we can see that when the angle is 90° (vertical), the ΔToF is null, as expected. By isolating the velocity as a function of the ΔToF , which is the measurable quantity, one obtains:

$$v_m = \frac{3}{16} \frac{c^2 \tan \alpha}{R} \Delta T \quad (14)$$

To write the ΔToF as a function of the flux Φ ,

$$\Phi = \iint_S v(x, y) dA = \int_0^R 2\pi r v(r) dr = 2\pi R^2 v_m \int_0^1 s v(s) ds = \frac{1}{2} \pi R^2 v_m \quad (15)$$

And the flux can be easily written as a function of the time difference:

$$\Phi = \frac{3\pi R c^2 \tan \alpha}{32} \Delta ToF \quad (16)$$

On the other hand, we can also consider the case in which the flow goes through a rectangular cross-section W times H in which the y direction is much shorter than the x direction ($W \gg H$), the velocity distribution is in the vertical direction, but can be written the same as 12 but in Cartesian coordinates. We will take that the height of the rectangular cross-section H is $H = 2a$

The ΔToF for the rectangular case is almost identical and can be written as:

$$\begin{aligned} \Delta ToF = t_{UPS} - t_{DNS} &= \frac{4a}{c \sin \alpha} \int_0^1 \left(1 + \frac{v}{c} \cos \alpha\right) ds - \frac{4a}{c \sin \alpha} \int_0^1 \left(1 - \frac{v}{c} \cos \alpha\right) ds \\ &= \frac{8a \cos \alpha}{c^2 \sin \alpha} \int_0^1 v ds \end{aligned} \quad (17)$$

and using the velocity distribution,

$$\Delta ToF = \frac{8H \cot \alpha}{3c^2} v_m \quad (18)$$

If we are interested in the ΔToF as a function of the flux:

$$\Phi = \iint_S v(x, y) dA = W \int_0^H v(y) dy = WH v_m \int_0^1 (1 - s^2) ds = \frac{2}{3} WH v_m \quad (19)$$

, and by taking the inverse, we get the maximum velocity as a function of ΔToF :

$$v_m = \frac{3}{8} \frac{c^2 \tan \alpha}{H} \Delta T \quad (20)$$

We can see that the result is identical as in the circular cross-section, only by changing the height H for the diameter $2R$. And the flux can also be easily written as a function of the time difference:

$$\Phi = \frac{W c^2 \tan \alpha}{4} \Delta ToF \quad (21)$$

To measure the flow, we must place the two transducers must be places at different points of the trajectory of the flow, such as in figure 2a. By measuring the transit time in both directions applying the above equations, the velocity or flux of the fluid can be obtained.

2.2.2.2 Doppler Effect The Doppler Effect is a consequence of a wave hitting a moving object. Consider a wave of frequency f which propagates at a velocity c . When it hits an object moving at a velocity v , in the same direction as the wave, from the point of view of the moving object, the crests of the wave are further from each other than what they really are. If, additionally, the wave is incident at an angle α with respect to the trajectory of the fluid, the observed frequency is $f' = \frac{c+v \cos \alpha}{c} f$, and the frequency shift is

$$\Delta f = 2 \frac{\Delta v}{c} f \cos \alpha \quad (22)$$

The factor 2 multiplying at equation 22 comes from the fact that the particle already receives the signal with a frequency shift, and then the receiver senses a signal with twice the original shift. With this, if an ultrasonic wave propagating in water hits an object such as an air bubble or another particle, it can be possible to obtain the velocity of the fluid by sensing the reflected wave and detecting the frequency-shifted signal by placing the receiving transducer in the opposite side of the tube, as in figure 2b.

2.3 Signal processing techniques

2.3.1 In-phase and Quadrature demodulation

If the received signals are acquired and digitalized properly, a sinusoidal pulse of frequency f , sampled at a rate of f_s at the ADC, should be obtained. For practical purposes, it needs to be down-sampled to be sent to the CPU. However, we do not want to lose any information. In-phase and Quadrature demodulation is an easy and practical method to down-sample this signal by changing the information to a lower frequency.

Taking into account the following property,

$$\cos \alpha \cos \beta = \frac{1}{2} (\cos(\alpha + \beta) + \cos(\alpha - \beta)) \quad (23)$$

one can take the sampled signal $x[t] = A \cos[2\pi f t]$ and a reference signal $r[t]$ at a frequency $f' = f - f_i$, being f_i the intermediate frequency, and the resulting product is:

$$re[t] = x[t] \cdot r[t] = A \cos[2\pi f t] \cdot \cos[2\pi(f - f_i)t] = \frac{1}{2} A \cdot (\cos[2\pi(2f + f_i)t] + \cos[2\pi f_i t]) \quad (24)$$

and doing the same with the reference signal dephased 90° :

$$\begin{aligned} re[t] &= x[t] \cdot r_{90^\circ}[t] = A \cos[2\pi f t] \cdot \cos[2\pi(f - f_i)t + \frac{\pi}{2}] \\ &= \frac{1}{2} A \cdot (\cos[2\pi(2f + f_i)t + \frac{\pi}{2}] + \cos[2\pi f_i t - \frac{\pi}{2}]) \end{aligned} \quad (25)$$

In both cases, it results in the sum of two sinusoidal signals, one at the intermediate frequency f_i and the other one at a frequency $2f + f_i$. If then this signal is processed with a low pass filter, it results in having the same information but at a lower frequency, although with half of the amplitude. Then, it can be decimated and treated easily, as less amounts of data have to be processed.

2.3.2 Sinusoidal phase estimation

The received signal after after sampling in the time domain is $s(t) = A \cos(2\pi ft + \phi)$. Consider also a normalized reference signal of the same frequency but with zero phase $r(t) = \cos(2\pi ft)$. To produce the demodulation, the received signal must be multiplied, on the one hand, by the reference signal but dephased 90° , and the other one by the original reference signal $r(t)$.

$$re(t) = s(t) \cdot r(t) = A \cos(2\pi ft + \phi) \cdot \cos(2\pi ft) = \frac{1}{2}A \cdot (\cos \phi + \cos(2 \cdot 2\pi ft + \phi)) \quad (26)$$

$$im(t) = s(t) \cdot r_{90^\circ}(t) = A \cos(2\pi ft + \phi) \cdot \cos(2\pi ft + \frac{\pi}{2}) = \frac{1}{2}A \cdot (\sin \phi + \sin(2 \cdot 2\pi ft + \phi)) \quad (27)$$

If now we take $s(t)$ and $r(t)$ as vectors in the digital domain, as is done in ?? with N samples $s[n]$ and $r[n]$, $0 \leq n \leq N - 1$, by making the dot product in equations 26 and 27, then the results are the averages, which are $\cos(\phi)$ and $\sin(\phi)$. Hence, we can estimate the phase between the sensed signal and the reference signal as

$$\tan \hat{\phi} = \frac{\sum_{n=0}^{N-1} s[n] \cdot \cos[2\pi fn + \frac{\pi}{2}]}{\sum_{n=0}^{N-1} s[n] \cdot \cos[2\pi fn]} \quad (28)$$

If we also consider that the received signal has a certain additive noise, characterized as a White Gaussian $w[n]$ with variance σ^2 , then the variance of the estimation is

$$var(\hat{\phi}) = \frac{1}{N \frac{A^2}{2\sigma^2}} = \frac{1}{N \cdot SNR} \quad (29)$$

where the Signal to Noise Ratio (SNR) can be calculated as $SNR = \frac{A^2/2}{\sigma^2}$.

3 Developement of the measurement system

As stated earlier, the goal of the project is to measure the velocity of water flowing through a pipe. The required range of speed measurement is from 0.2 to 200 cm/s, according to the needs of the current research project. The two considered options to carry out the flow meter are to use either the Δ Time of Flight or the Doppler Effect methods. Fortunately, the required hardware for both methods is very similar. Hence, both of them can be tested. Beforehand, however, an analysis of the requirements of both methods must be made. To perform the measurements, the system will be based on a Red Pitaya STEMLAB 125-14 computer board. It is a single board computer based on a Dual core ARM cortex A9 and FPGA which can run on a Linux Operating System, and two 14 bit 125 Msamples/second ADC and DAC. It communicates to the exterior via an Ethernet cable.

3.1 Measurement methods

3.1.1 Time of Flight

In this method, the magnitude to measure is the difference in transit time between the upstream and downstream propagation signals. As equation 14 and 20 prove, the velocity of the fluid is proportional to the time difference. Hence, a method for resolving with enough resolution is needed. For the lowest speed, which is 0.2 cm/s, it is equivalent to a Δ ToF of the order of 50 ps by using equation 20. With the used ADC and hardware, the highest sampling frequency that can be used is 1.25 MSamples/second, which means a T_s of 8 ns. Hence, with a peak detection or zero-crossing algorithm, it is not possible to obtain the required resolution.

An alternative is to use a phase detection algorithm based on In-Phase and Quadrature demodulation, which has been described in Section 2.3.2. According to equation 29, with a high enough SNR and long enough signal, one should be able to get the required resolution, as long as $\frac{var(\phi)}{2\pi f}$ is significantly lower than the minimum Δ ToF needed.

3.1.2 Doppler Effect

To detect the velocity of the fluid with the principle of the Doppler Effect, the main drawback is that some heterogeneity is needed in the flow in order for the sound wave to reflect and be emitted in a different direction [10]. However, this can be achieved with air bubbles or by mixing water with some other substance, like a saline solution. As equation 22 shows, to get the velocity, the magnitude needed is the frequency shift of the reflected signal with respect to the transmitted signal. To get the resolution of 0.2 cm/s, the resolution in frequency should be of around 1.3 Hz with an angle of $\alpha = 60^\circ$, according to equation 22. To achieve this resolution, the duration of the acquired signal (the window) must be long enough. The longer the signal is in the time domain, the smaller each step of the frequency domain will be when the FFT algorithm is applied. The resolution in frequency domain is given by the following equation:

$$\Delta f = \frac{f_s}{N} \quad (30)$$

3.2 Instrumentation

The model of the used transducers is US0014-001 from Audiowell. The information on the *datasheet* is very scarce and the only relevant aspects are:

- Resonance frequency of 975 ± 30 kHz
- Resonant impedance lower than 110Ω
- Static capacitance $1150 \pm 20\%$ pF
- Suggested driving voltage of 5 V peak to peak

With these requisites in mind, the hardware and software has to be built. Figure 3 shows the different systems of the sensor.

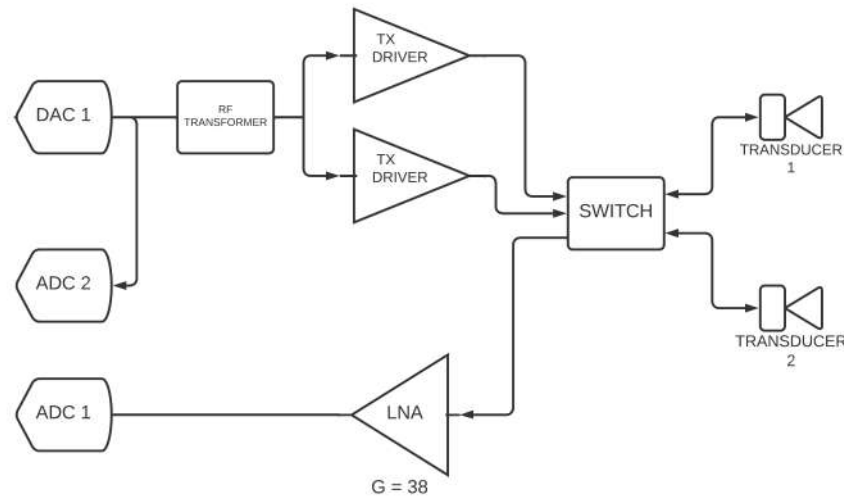


Figure 3: Block diagram of the different components of the flow-meter

- a pulse generator
- a driver to amplify the pulsed signal and increase the current at the input of the TX transducer
- an instrumentation amplifier to process the signal received by the RX transducer
- an analog switch to change the function of the transducers from TX to RX and vice versa
- ADC

3.2.1 FPGA

The first step in the process is to be able to send pulsed sinusoidal signals with the Red Pitaya board. To do this, the best solution is to make use of the open-source codes posted

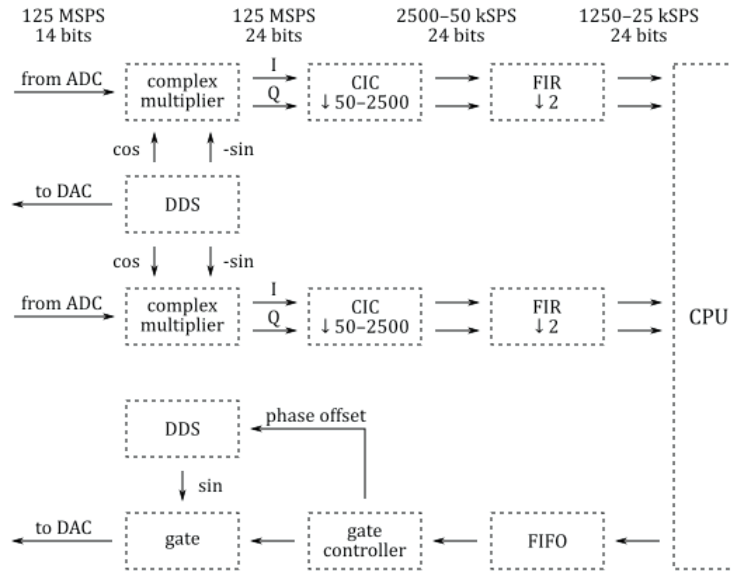


Figure 4: FPGA block diagram [11]

in GitHub by the developer Pavel Demin. It extensively uses the FPGA to generate the pulses, as well as to do the first part of the digital signal processing. This project was designed for a pulsed nuclear magnetic resonance application, but most of the components are useful for the ultrasonic sensor. The FPGA takes care of both pulse generation and data acquisition and processing.

3.2.1.1 Pulse generation A DDS (Direct Digital Synthesizer) compiler is a software-controlled sinusoidal generator based on a Phase Generator and a SIN/COS Lookup Table. It generates, as seen in the lower part of Figure 4, a sinusoidal signal based on a phase offset which is set by the CPU. Then this signal is fetched by a gate which controls when to send the signal, in order to generate the pulses, and finally goes through the DAC to be converted to the analog domain. The amplitude of the pulses can be controlled by the software, with a maximum peak to peak voltage of 1.8 V.

3.2.1.2 Data acquisition and further processing The DDS also generates, as seen in Figure 4, a cosine and a sine of frequency f_i , which are multiplied by the signals coming from the ADCs, to demodulate the signal at an intermediate frequency f_i , as has been detailed in section 2.3.1. Then both I and Q components are decimated between the rates of 50 to 2500. This means that, by using the minimal decimation, the final sampling rate is 2.5 MS/s and with the maximum, 50 KS/s. In order to avoid aliasing, f_i must be low enough. Finally, the FIR filter makes sure all the frequency components that are not of interest, are removed, and the data is sent to the CPU. The FPGA has barely been modified. Only a LED has been configured to blink when the FPGA is running, by modifying the block design in the Vivado IP Integrator.

3.2.2 Signal driver

In order for the transmitting transducer to emit a strong sound wave, the input electrical signal must be powerful enough. The analog signal comes from the DAC, which has a low impedance output (50Ω), a maximum of 1.8 V of amplitude and is asymmetric. To drive the transducer, the *datasheet* of the transducer [12] suggests an amplitude of 5 V peak to peak, and indicates that the impedance at the resonant frequency is lower than 110Ω .

3.2.2.1 Differential line driver Initially, the intention for building the driver was to use a MOSFET Driver. However, none was easily available on the market, and we decided to use a MAX4147 differential line driver instead. This model is obsolete; nonetheless, the research group still has a few old boards containing this chip, and we decided to reuse the boards, which had been used as pre-amplifiers in the context of a former research project. All the instrumentation in this project works with a supply voltage of $\pm 5V$.

As stated in the *datasheet* [13], the MAX4147 is "optimized for differential, high-output-current applications", which is exactly the need for the transducer, and "the MAX4147 drives $\pm 2.6V$ into a 26.5Ω load, or $\pm 5.6V$ to a 53Ω load". The 110Ω of the transducers in balanced mode can be thought of as being split in $2 \cdot 55 \Omega$, thus representing a 55Ω load for each of the two symmetric outputs. However, some additional loss of signal occurs in the switching board, imposing a certain voltage drop which must be accounted for when selecting the output resistors.

3.2.2.2 RF transformer Another aspect to take into account is that the output of the DAC is unbalanced, and this means that there has to be an AC/AC transformer between the DAC and the balanced inputs of the driver. For this purpose, the first approach is to make what is commonly known as a *balun*. As can be seen in Figure 5, two coils with N_1 and N_2 turns are wound on a ferrite ring, and on one end there is the unbalanced signal, and on the other end, the balanced signal. With the ratio N_1/N_2 , the output impedance and the size of the ferrite ring, one can adjust the voltage gain and the frequency-band of useful operation. The inductances L_1 and L_2 are proportional to N_1^2 and N_2^2 , respectively.

For a given Z_2 , N_1 and L_2 , the input impedance Z_1 is ([14]):

$$Z_1 = j\omega L_1 + \frac{k^2 L_1 L_2 \omega^2}{j\omega L_2 + Z_2} \quad (31)$$

where k is the coupling factor. When the output impedance is low enough

$$|Z_2| \ll |j\omega L_2|, \quad (32)$$

one can develop the Taylor series until order 1 of $(1 + \frac{Z_2}{j\omega L_2})^{-1}$ and get the following result:

$$Z_1 = j\omega L_1 - jk^2 \omega L_1 (1 - \frac{Z_2}{j\omega L_2}) = j\omega L_1 (1 - k^2) + Z_2 \frac{L_1}{L_2}. \quad (33)$$

When the coupling factor is assumed ideal or almost, then $1 - k^2 \approx 0$ and we get that the input impedance is proportional to the ratio of inductances

$$Z_1 = \frac{L_1}{L_2} Z_2. \quad (34)$$

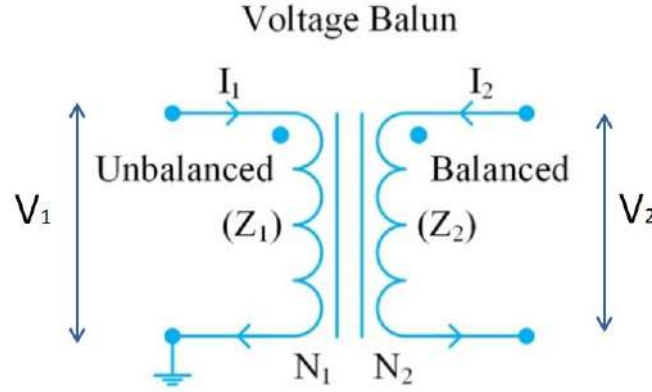


Figure 5: *Balun* schematic

Since the DAC is $50\ \Omega$ -terminated, the maximum power transmission occurs when there is impedance matching. Thus, under conditions of RF transmission (electrically long cables, etc) one usually aims at a $50\ \Omega$ termination. However, in this application no long cables were used and the receiving amplifier has comparatively high input impedance at the used frequency. Therefore impedance matching is not required for proper function and hence port 2 doesn't need to be terminated. This has the advantage of providing twice the voltage to the amplifier input than under matching conditions.

Furthermore, we can take into account that the power across the *balun* is conserved, that is,

$$P_1 = P_2 \implies \frac{V_1^2}{R_1^2} = \frac{V_2^2}{R_2^2} . \quad (35)$$

Moreover, with property 34 and $L \propto N^2$, then the voltage gain across the transformer, measured as the voltage difference at the output divided by the voltage at the input, is

$$G = \frac{V_2}{V_1} = \frac{N_2}{N_1} . \quad (36)$$

$$L = \frac{N^2 \mu_0 \mu_r A}{L} \quad (37)$$

With the values previously mentioned, a gain of 2 seems appropriate. A ferrite ring FT114-43 has been used. By taking a normal value of $L_1 = 100\ \mu F$, then $L_2 = 400\ \mu F$, and the values of A , L and μ_r of the used ring, with equation 37 we can set the number of turns $N_1 = 8$ and $N_2 = 16$.

3.2.3 Low Noise Amplifier

As the voltage provided by the sensing US transducer on US signal pickup is very low, it is necessary to apply an amplification stage with a low noise performance. Ideally, we would need an Instrumentation Amplifier with a voltage noise below $1nV/\sqrt{\text{Hz}}$. However,

the scarcity of available ICs in the market made us consider, again, to use old boards and modifying them. For the same project as the driver board, there was also an Instrumentation Amplifier PCB containing a pair of AD797 Operational Amplifiers, which are low noise ($0.9nV/\sqrt{Hz}$) [15], and the same differential line driver MAX4147. The circuit is shown in Figure 6. The first stage consists of two operational amplifiers in a non-inverting configuration, one for each side of the symmetric signal. The resistors are $R_F = 590\Omega$ and $R_G = 33\Omega$, giving a gain of $G_1 = 1 + \frac{R_F}{R_G} = 19$. Before the second stage, there is a low

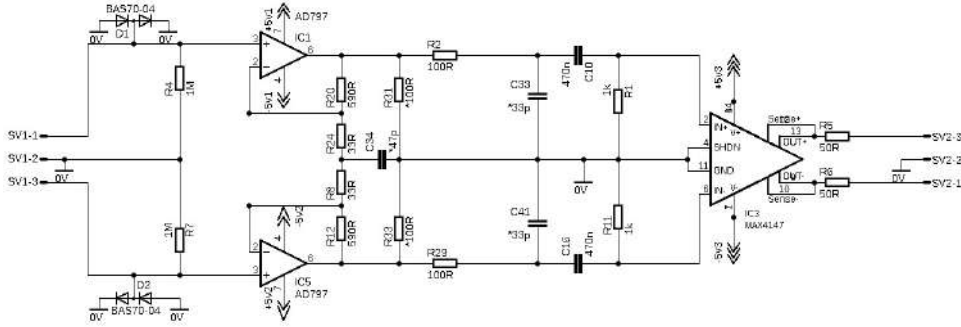


Figure 6: Schematic of the Low Noise Amplifier made with Eagle (Autodesk, Inc, USA)

pass filter of cut-off frequency 48 MHz and a high pass filter of 338 Hz, and thus do not affect the performance at 0.975 MHz.

The Differential Line Driver MAX4147 is the second stage of the amplifier and gives a gain of 2V/V, making a total gain of 38. If needed, it can be increased by changing the values of the resistors R_F and R_G . After this stage, the signal must go directly to the ADC. However, the ADC of the Red Pitaya is asymmetric. Another RF transformer could be used to convert the balanced signal into an unbalanced to enter the ADC. However, after making some tests with the transducers, it was seen that the signal of a single output terminal with respect to GND could perfectly serve as an asymmetric output. Hence, the second terminal was not used.

3.2.4 Switch board

To switch the function of the transducers from TX to RX and vice versa, an analog switch was needed. Since each transducer has two terminals, 4 channels were needed. The idea was to use the GPIO pins from the Red Pitaya board to control the switching. The FPGA already has implemented the hardware to access the digital pins from the client software.

Whilst looking for CMOS switches and multiplexers, we wanted one with as little ON-Resistance possible, minimum cross-talk, capable of working with signals of $\pm 5V$, and if possible, multichannel. Several chips with 5Ω were available on the market, but they were only available in TSSOP packages, which are too small to solder manually to a PCB. The best alternative we found was a MAX333A multiplexer with ON-Resistance $< 17\Omega$ [16]. It was not the optimal solution but enough for our application. On the positive side, this chip is TTL compatible, so the GPIO signal from the RP can be used directly to control the switches.

However, the maximum current on the switch terminals is 70 mA, which is enough for the RX signal coming from the receiving transducer, but not for the TX, because the driver can provide up to 160 mA. However, there is a solution: the MAX4147 has a pin, SHDN, that when is set to "high" mode, the output of the driver is high impedance, and no signal is output. This allows us to use two identical drivers, and enable and disable the SHDN pin alternatively on both chips such that when one is driving, the other one is in high impedance, and vice versa. Subsequently, the outputs of the two line drivers are connected directly to the two transducers. Both transducers are connected to the LNA through the switches. For instance, when the MAX4147 n°1 is driving the pulse, the transducer 1 emits this signal while the switch that connects T1 to RX is open, and the one connecting T2 to RX is closed. Since the driver n°2 is in high impedance, there is no collision between the signal coming from T2 with the one from TX2. To make sure that the high impedance state does not add noise to the RX signal, two Schottky diodes in opposite directions are added as isolators. Moreover, connecting TX1 and TX2 on the two inputs of the MUX

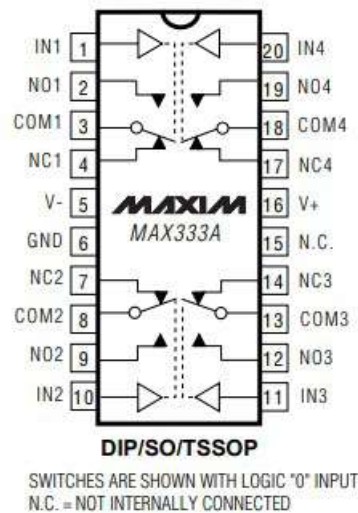


Figure 7: Pin configuration of MAX333A Analog Multiplexer

would cause cross-talk between them. The chip contains 4 different multiplexers. Hence, the best solution is to always leave one MUX input in high impedance, and use the 4 MUXes by connecting the RX on both sides. So, IN1 and IN2 receive the control signal for 1 side, and IN3 and IN4 the other. A PCB layout was designed with *Eagle* and printed, and then soldered the components. The schematic and layout can be found in the appendix B. The layout was specifically designed to avoid all possible cross-talk between the two signals, so on one side of the chip there are the connections to one driver and transducer, and on the other side, the connections to the other two. Also, COM1 and COM4 connect to the positive receiving end, and COM2 and COM3, to the negative receiving end. These channels then go through the LNA and to the ADC2. NO1 and NO2 are the positive and negative signals from one transducer, respectively, and NO3 and NO4, from the other. To have a safe high impedance at the unconnected pins, a $100k\Omega$ resistor between these pins and the ground is placed.

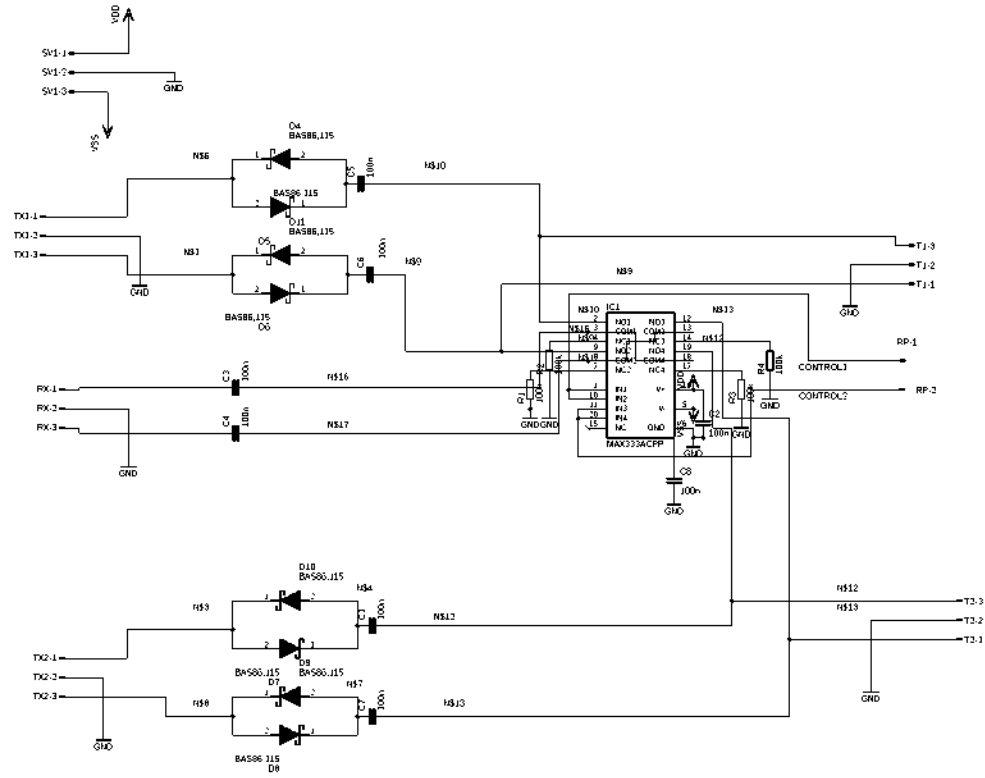


Figure 8: Schematic of 4 channel analog switch PCB

After testing the board, we have seen that in the pair of Schottky diodes, the voltage is dropped by 0.7 V. This means that at the output of the driving board, there should be a voltage of around 3.25 V to have 2.5 V at the transducers. Finally, a resistor of 25 Ω is placed at the outputs of the MAX4147 to achieve this. With everything, there is a voltage of 2.56 V peak to peak at each end of the transducer, so just a bit above 5 V in total, which was the requirement.

3.3 Noise analysis

To finish the hardware section, it is important to find how the minimum noise that the phase measurements can have due to noise in the instrumentation.

In the receiving end, the circuit has two stages in the LNA. Firstly, the two operational amplifiers and then the differential line driver. Since the circuit is symmetric, we will make the analysis only for one side. The voltage source, in this case, is the transducer, with an output impedance of $R_s = 55 \Omega$. The bias resistor of 1 M Ω in principle also contributes, so the effective source resistance is $R_s || R_{bias}$, but as $R_{bias} \gg R_s$, it can be neglected in the parallel circuit. First there is the AD797 in a non-inverter configuration. The *datasheet* specifies an input voltage noise of $E_{NI1} = 0.9nV/\sqrt{Hz}$, and current noise of $I_{BI1} = 2pA/\sqrt{Hz} = I_{BN1}$. In our case, $R_F = 590 \Omega$, $R_G = 33 \Omega$. Hence, the gain is

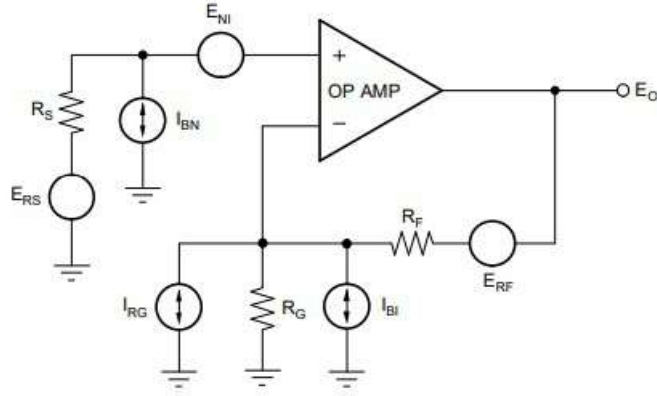


Figure 9: Op Amp noise analysis circuit [17]

$G_1 = 19$. The total output noise contribution per \sqrt{Hz} is given by the following equation:

$$E_{o1} = \sqrt{(E_{NI1}G_1)^2 + (I_{BN2}R_SG_1)^2 + 4kTR_SG_1^2 + (I_{BI}R_F)^2 + 4kTR_F + 4kT\frac{R_F^2}{R_G}} \quad (38)$$

In the second stage of the LNA, we have to consider the noise from all the resistors, the noise current and voltage input noise, and the output noise of the first stage, multiplied by the gain of the second stage. Thus, since the gain of the first amplifier is much larger than the one of the differential line driver, we also expect the noise contribution to be larger. The MAX4147 has a voltage input noise of $8nV/\sqrt{Hz}$ and current noise $I_{BI2} = 1.7pA/\sqrt{Hz}$ for all frequencies above 10 kHz.

With that, the total noise at the output of the second stage will be:

$$E_{o2} = \sqrt{2(E_{o1}G_2)^2 + 4kTR_2G_2^2 + E_{NI2}^2(\frac{G_2}{2})^2 + I_{NI2}^2(R_2||R_1)^2} \quad (39)$$

The feedback term here it is not added, as it is due to the internal resistors and is included in the value of I_{NI2} and E_{NI2} .

Moreover, we need to take into consideration the quantization error of the ADC, given by the value of the Least Significant Bit = Voltage Range / 2^n , being n the number of bits:

$$E_{ADC} = \frac{LSB}{\sqrt{12}} \quad (40)$$

However, this is considering the full spectrum of the ADC, which is 125 MHz. Since we are only using a small part, the factor $\sqrt{Bw/125MHz}$ must be multiplied.

The minimal bandwidth of our system is given by the synchronous demodulation, which is $1/T$, which is the inverse of the pulse length. In this system: 200 ms, which is equivalent to a bandwidth of 5 Hz.

All together, $E_{o1} = 28nV/\sqrt{Hz}$, and $E_{o2} = 80nV/\sqrt{Hz}$. We have shown that, although the gain of the first stage is 10 times larger than of the second stage, since the MAX4147 has a much larger noise than the AD797, their contributions are comparable. The quantization error is $3.15nV/\sqrt{Hz}$. Hence, the resolution of the ADC is high enough to not affect significantly the total noise. In conclusion, the total noise can be expressed as $V_n = \sqrt{E_{o2}^2 + E_{ADC}^2} \cdot \sqrt{bw} = \sqrt{80^2 + 3^2}nV/\sqrt{Hz} \cdot \sqrt{5Hz} = 0.18 \mu V$.

The expected variance of the phase can be obtained from equation 29 when calculating the SNR of the measured voltage signal. To do that, we measure the amplitude of the pulse at one output of the receiving transducer. It has been done in the case in which there is less amplitude, to obtain the worst case scenario. The measured amplitude is $2mV$. We obtain $SNR = \frac{A^2}{2\sigma^2} = \frac{(2mV)^2}{2 \cdot (0.18\mu V)^2} = 61.7 \cdot 10^6 = 77.9dB$ and a $var(\hat{\phi}) \approx 10^{-13}$. When converting into time, we take the square root to use the standard deviation, and it equals $10^{-13} s$, and in velocity, $1.3 \cdot 10^{-4} cm/s$, which is well below the requirements. This shows that the noise due to the pre-amplifiers should not limit the resolution of the flow-meter.

4 Software development

The complex software to run the FPGA correctly has been adapted from Pavel Demin's Red Pitaya Guide [11] and Tobias Trimmel's Bachelor's Thesis on Pulsed NMR [18]. It runs partially on the Red Pitaya board and on a personal computer. It consists of a server-client architecture. The client is a C code running on the Red Pitaya's Linux and is responsible for sending the correct data to the FPGA to generate the pulses and receive the sampled data. The client application runs on the personal computer and is drafted in the programming language Python. The two applications communicate by a socket connection via Ethernet.

4.1 Server application

The C code running on the Red Pitaya is responsible for sending to the Red Pitaya the data needed by the FPGA to run the hardware, and it has not been modified from the original version. It sends the sampling rate, the pulse length, the time to repetition, the evaluation range, the number of samples, the pulse amplitude, the frequency of the emitted pulses and the intermediate frequency for I-Q demodulation to the FPGA. To do that, the code maps these different variables with the registers of the FPGA with their address, which can be found by building the FPGA project with Vivado. As can be seen in Figure 10, there are 4 registers. The first one, *sts* stores some control data; *cfg* stores the general data for the acquisition and transmission signals, which are a reset signal, the intermediate frequency f_i , the sampling rate for the down-sampling and the pulse amplitude and frequency. On the other side, in *rx_data*, it stores the received data from the ADC; in the *tx_data* it stores the data for each one of the pulses that the client orders to send.

```

1  sts = mmap(NULL, sysconf(_SC_PAGESIZE), PROT_READ|PROT_WRITE, MAP_SHARED,
    fd, 0x40000000);
2  cfg = mmap(NULL, sysconf(_SC_PAGESIZE), PROT_READ|PROT_WRITE, MAP_SHARED,
    fd, 0x40001000);
3  rx_data = mmap(NULL, 16* sysconf(_SC_PAGESIZE), PROT_READ|PROT_WRITE,
    MAP_SHARED, fd, 0x40010000);
4  tx_data = mmap(NULL, 16*sysconf(_SC_PAGESIZE), PROT_READ|PROT_WRITE,
    MAP_SHARED, fd, 0x40020000);
5
6  rx_rst = ((uint8_t*)(cfg + 0));
7  rx_freq = ((uint32_t*)(cfg + 4));
8  rx_rate = ((uint16_t*)(cfg + 8));
9  tx_level = ((int16_t*)(cfg + 10));
10 rx_cntr = ((uint16_t*)(sts + 12));
11
12 tx_rst = ((uint8_t*)(cfg + 1));
13 tx_freq = ((uint32_t*)(cfg + 12));
14 tx_cntr = ((uint16_t*)(sts + 14));

```

When the pulse sequence starts, the acquisition starts as well and sends the received data stored on the rxdata register back to the client software via the socket communication.

Data (32 address bits : 0x40000000 [1G])						
cfg_0	S_AXI	reg0	0x4000_1000	4K	▼	0x4000_1FFF
rx_0/reader_0	S_AXI	reg0	0x4001_0000	64K	▼	0x4001_FFFF
sts_0	S_AXI	reg0	0x4000_0000	4K	▼	0x4000_0FFF
tx_0/writer_0	S_AXI	reg0	0x4002_0000	64K	▼	0x4002_FFFF

Figure 10: Registers in the FPGA

4.2 Client application

The client application is implemented on Python is a modification of the original code. The length of the pulses is set to 50000 samples. It can be changed, although longer pulses can generate problems. The program works the following way: first it connects to the server application via a Socket connection. Once the user presses the *Start* button, one pulse of configurable duration and frequency is sent. Then, as soon as the server has received the data, it is sent back to the client and read in the *read_data* function. The data is first stored in a buffer and then assigned to the variable *self.data*. It consists of a 128 bit float type containing the real and imaginary parts of both channels, which come from the I and Q components of the demodulation carried out in the FPGA. In the original software, only the real part of the first ADC was used, so without any documentation of how the software worked, it was hard to know how to use both ADCs and I and Q components. In a communication in Pavel Demin's Forum, he provided the key information, which is depicted in Figure 11. It is of crucial importance for the development of the algorithm.

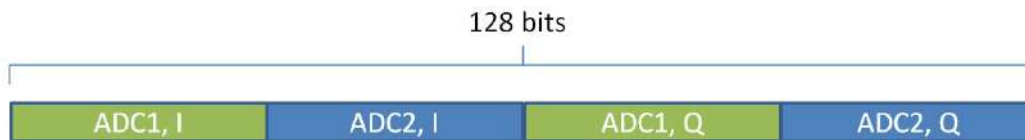


Figure 11: Data structure after reading from buffer

Once we have in four different variables the real and imaginary parts of both channels, the data is processed in another function, where the sinusoidal phase estimation method described in the theoretical section is applied, and the phase of the real part of the received signal is calculated, using the I and Q components of the channel 2 as reference for the algorithm. This process is repeated as many times as the user sets. The software is set to control the switches by changing the values of the GPIO pins. The way in which we did the measurements consists of sending two pulses in one direction (T1 to T2), and then changing the switches. Then, two more pulses (T2 to T1) are sent and the process is repeated as many times as one wishes to create an averaging. Then, one can also set how many averages are carried out. Moreover, the program waits for a certain amount of seconds, so the user can change the flow with the pump and wait for the transient to end,

which should not be more than a few seconds. Also, this can be repeated as many times as the user wants, and can be set in the Graphical User Interface (GUI) seen in Figure 12.

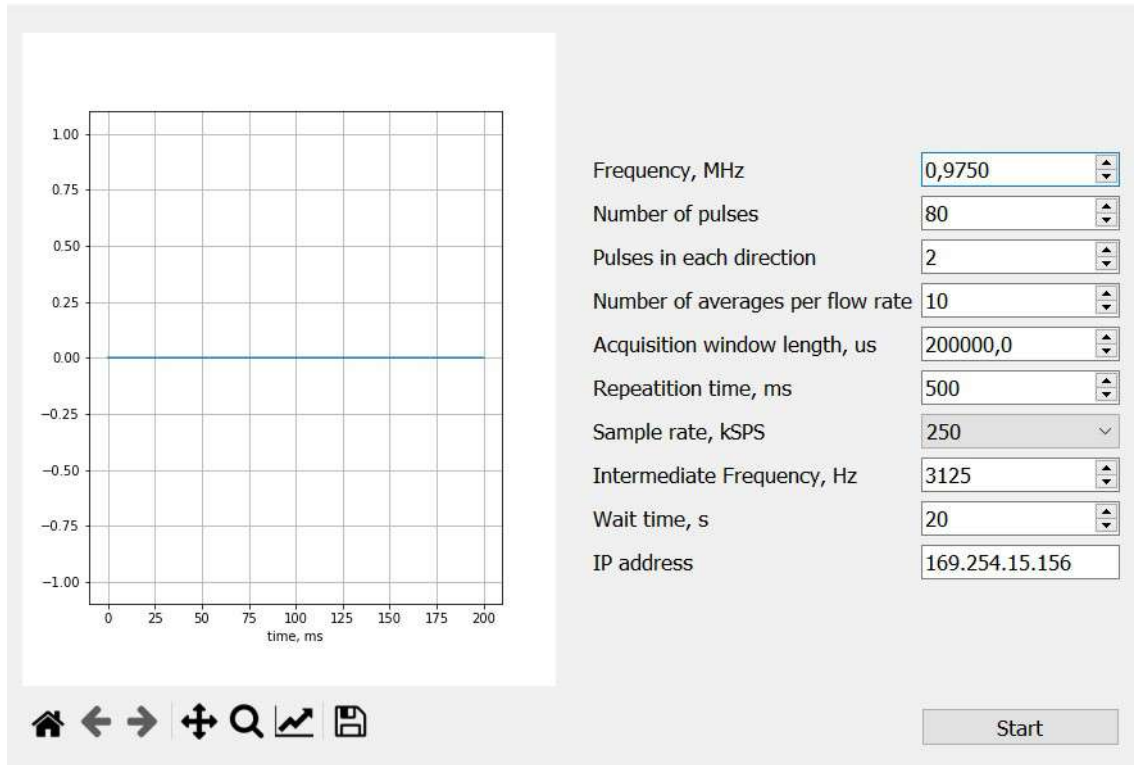


Figure 12: Graphical User Interface

4.3 Program flow

The interaction between server and client applications can be shown in Figure 13.

4.4 Options and limitations

As stated above, the FPGA allows to down-sample the 125 MS/s signal to 25 kS/s, 50 kS/s, 125 kS/s, 250 kS/s, 500 kS/s, 1250 kS/s and 2500 kS/s. In principle, the best should be to use the highest sampling rate. However, the socket communication has certain limitations, and with the 2.5 MS/s option, invalid measurements occur due to a high probability of package loss. The option of 1.25 MS/s works for short pulses, of the order of 10 to 50 μ s. However, for pulses long enough, since the probability of package loss is still considerable, several sets of data are lost. With many tests, we have concluded that for 200 ms-long pulses, the optimal sampling frequency is 250 kHz. If the IF is too high, there might be aliasing. If it is too low, it might interfere with the DC component. The bandwidth for 200 ms pulses is very small. Hence, any value below $f_s/2$ and a few Hz should work. An IF value of 3125 Hz has been used. Different values have been tried and the performance does not change.

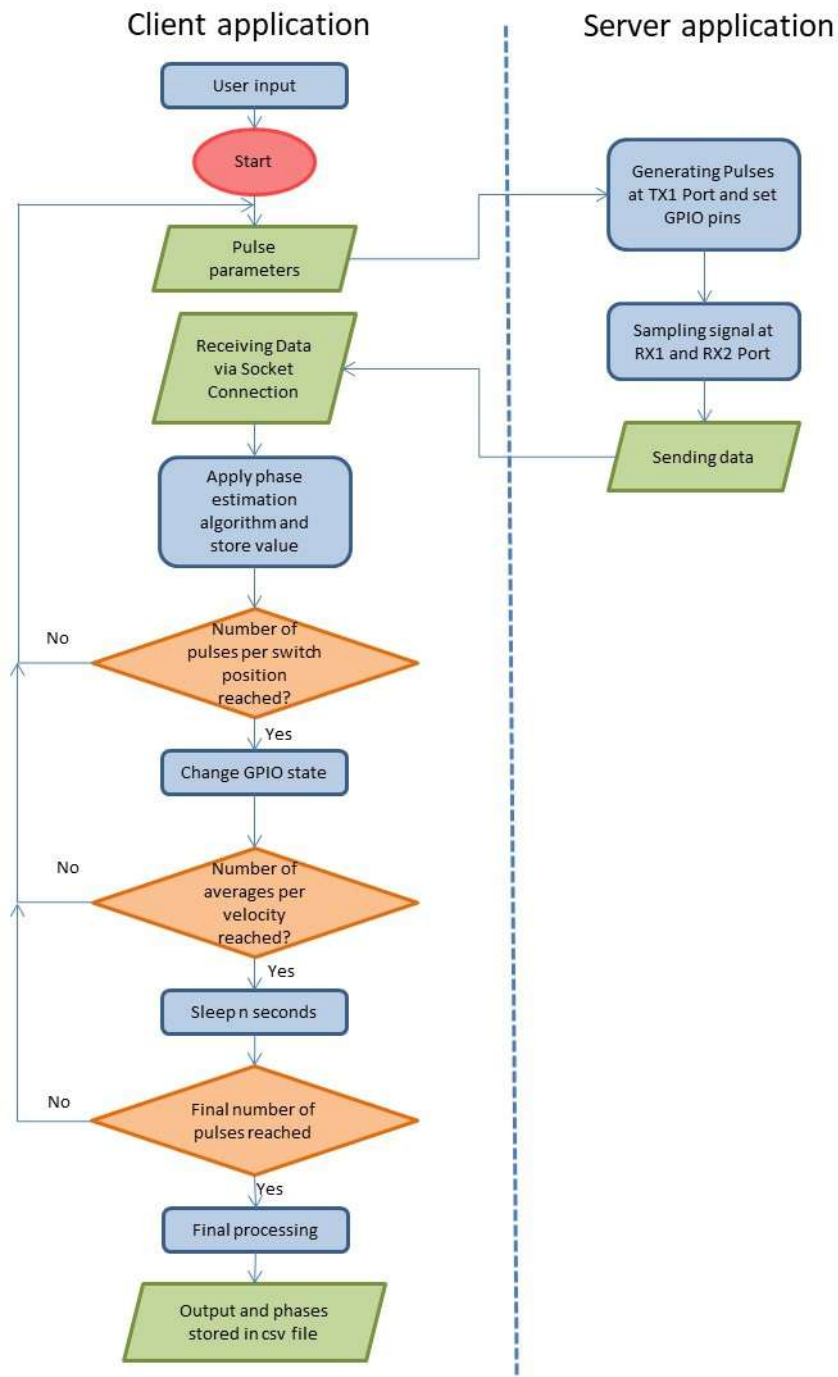


Figure 13: Flow diagram of the software

5 Measurements, results and discussion

In this section of the thesis, a complete description of the measurements taken will be done. Because of all the different studies and cases, each case will be analysed separately and followed by a discussion commenting the results. It has been written in such a way so that each one of the different studies is motivated by the previous one. However, first on sections 5.1 and 5.2, some preliminary measurements will be done to make sure the algorithms and hardware work correctly.

5.1 Phase estimation algorithm verification

The first step would normally consist in trying to measure the change in time of flight upstream and downstream. To do this, the preferred method would be to measure the phase of the sampled signal with respect to a reference signal. However, first it was important to see if the developed algorithm, based on equation 28 worked properly with wire length measurements. Also, we would like to check experimentally the variance of the phase measurements.

To carry on the test, the measurements consisted in connecting the DAC of the Red Pitaya board with one of the ADCs with coaxial cables of different lengths. Since the propagation velocity of the signal through a coaxial cable is around $2 \cdot 10^8$ m/s, cables of different lengths would have a different transit time, and hence a different phase.

However, comparing two coaxial cables with a length difference of 50 cm, no good results were found. The phase was calculated with respect to a purely synthetic sinusoid with the same frequency generated on the host PC. Looking in detail in the signals we found that the received data has a jitter of up to three samples, which corresponds to at least $1/f_s = 4$ ns using a sampling frequency of 250 kS/s. Since the target resolution is around 50 ps, it is unacceptable. As both ADCs work from the same clock, their differential jitter is zero and the problem can be solved. To solve it the second ADC was used as the reference by measuring the TX signal via a T-junction. The reference cable, connected to ADC 2, served as reference for the other one, and several measurements with different lengths were tested. The expected time difference is trivial to calculate:

$$\Delta t = \frac{\Delta length}{c} \quad (41)$$

By using two different coaxial cables a length difference of 4 cm, a phase difference of $1.33 \cdot 10^{-3}$ rad has been found by making 100 measurements with each cable and taking the average value, which corresponds in a $\Delta T = 218$ ps and a distance of 4.36 cm. The phases can be seen in Figure 14. Taking into account that both cables are different and might not have the exact same propagation velocity, we can conclude that the algorithm works. The standard deviation of the phase with each different cable has been calculated and is approximately 10^{-5} rad for both of them.

On the other hand, to check if the measured data obeys equation 29, we need to determine the SNR. To characterize the transmitted signal, and to know the variance of the noise, we only need to connect a 50Ω terminator to an ADC, sample with the ADC during the

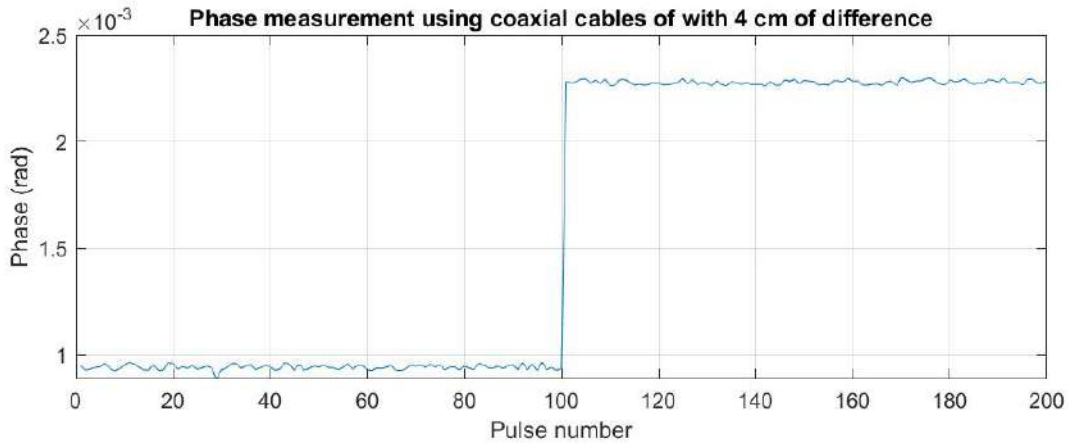


Figure 14: Phase of received pulses with two different coaxial cables

length of the window and calculate its standard deviation. For the amplitude, we can take the same as in section 3.3, which is 2 mV, so a comparison can be done.

The standard deviation of the received signal when using a 50Ω terminator is $\sigma = 30\mu V$. This is an unexpectedly high value, to which we have no explanation for. It means that the noise at the input stage of the Red Pitaya is extremely high. It could be due to operational amplifiers with high noise before the ADC, or cross-talk with the digital circuit. Nevertheless, we can calculate how it affects the standard deviation in velocity. Thus, $SNR = \frac{A^2}{2\sigma^2} = 2220 = 33.4dB$. Applying equation 29 for a pulse of length 50000 samples, theoretically we would get $var(\phi) = \frac{1}{N \cdot SNR} = 4.5 \cdot 10^{-14}$ ($\sigma = 2 \cdot 10^{-7}$), and therefore a standard deviation in velocity of 0.02 cm/s. This shows that the noise due to the input stages of the Red Pitaya is of the order of 1000 times larger than due to the pre-amplifiers, which has been analyzed in section 3.3. Nonetheless, it is still below the limit that we want to obtain.

5.2 Interference reduction

During the first measurements, a 1.5 meter long twisted pair was used to carry the signal from the driver to the transducers. However, before submerging the transducers in water to make the first tests, it was observed that there was a significant cross-talk between them, with an amplitude of 60 mV.

There could be different explanations for that, and easy to check. The first hypothesis was that it was just acoustic signal that can propagate weakly through air. However, when moving the transducers further apart and pointing to different directions the signal did not change. Hence this hypothesis was ruled out.

The other option was that the twisted pair does not fully shield the two pairs of wires, even though in theory it should, as the one being used was a Shielded Twisted Pair (STP). We removed one transducer and soldered it into another twisted pair, and repeated the measure. Surprisingly, the cross-talk was reduced to a 10% of the original amplitude, as can be seen in Figure 15. In conclusion, the twisted pair does not completely shield the

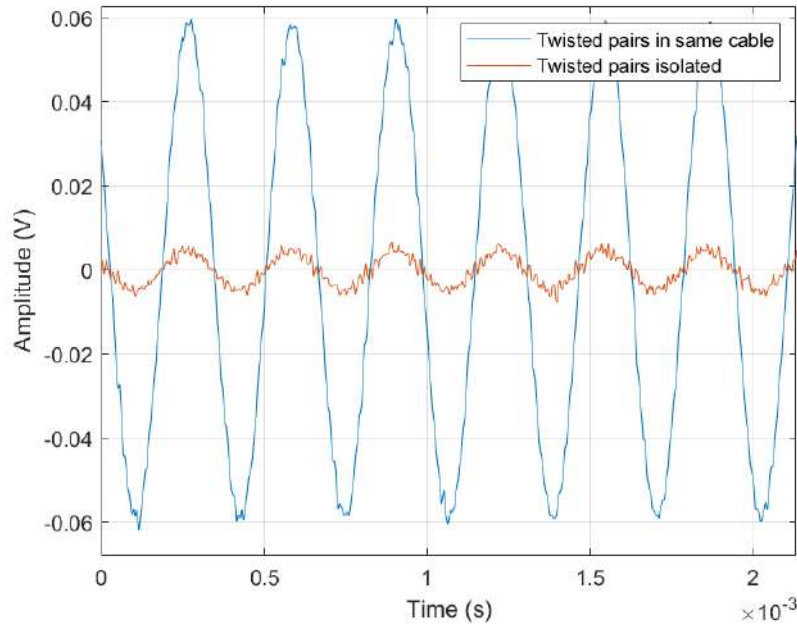


Figure 15: Cross-talk whilst using neighboring twisted pairs in the same cable (blue) and twisted pairs in different cables (isolated)

two pairs of wires, and to obtain the best signal quality it is best to use two different pairs to connect them to the signal driver and LNA.

5.3 Velocity measurements in a 24 mm PVC tube

5.3.1 Measurements with phase shift

Once the previous method was validated, the next step was to begin with flow measurements. A first set-up was assembled to test both Δ ToF and Doppler methods. Furthermore, with the help of 3D printed models, the transducers can be attached to improve the comfort and repeatability of the measurements.

The set-up consists, in the first place, the pump *Centrifugal Pump MultiFlow* from gaMPT, shown in Figure 16, which can create a flow of water from 0 to 8.8 liters per minute. The 7 segment displays of the pump can read the flux it is pumping, with a resolution of 0.1 liters per minute, which can be changed manually by turning a knob. The water entering the pump comes from a water tank with the output adapted to connect a gardening hose. The hose that is integrated in the pump has a diameter of 15 mm, which is thinner than the one which we want to use to measure. Hence, with an adapter and a few plastic clamps, it is connected to the desired tube, with a diameter of 24 mm, which better fits the transducers. The water flowing out of the measuring tube then goes back to the water reservoir. **All the measurements in this thesis are referenced to the flow value given by the pump.** Note that the pump can be calibrated in one point, with a defined flow while collecting the water during a certain time and measuring its volume.



Figure 16: Centrifugal Pump used for all the measurements in this project.

The other point is zero flow, and the controller in the pump computes a linear regression. However, we do not know if the actual behaviour is linear, and this might cause some inconsistencies in the results and difficult the repeatability of measurements. However, as an accurate reference flow-meter was not available, this procedure was maintained.

For these measurements, the idea was first to try to send and correctly receive the pulses in both directions and try to see if it is possible to detect any difference in time of flight. A provisional board with relays was built to use as switch. The two transducers were clamped to the tube with small plastic tubes that were cut in order to make a good adaptation between the transducers and the measuring tube. Only one was glued to the tube, so the other can be moved around to find the best position to be attached. The space between the transducer and the tube wall was filled with grease to improve transmission and coupling. For these first measurements, a grease used for lubricating machinery was used. For the rest of the measurements, the synthetic grease *SuperLube Mutlti-purpose synthetic grease* with PTFE was used, as recommended in [19].

Once the signal was properly received on the RX transducer, a support structure was 3D printed with an Ultimaker S5 printer.

The first attempt to calculate the time of flight consisted in sending 20 pulses from T1 to T2, then changing the state of the switch, and send 20 more pulses. This was repeated for different flow values: 0, 1, 2, 3, 4, 5, 6, 7, 8 and 8.8 l/min. Results show that for low flow rates, a time of flight difference was found. However, for higher velocities, the phase estimation was very noisy. The absolute measured phase for all the measurements can be seen in Figure 18, and counterintuitive phenomena were observed:

- Even when the flux is zero, there is a phase difference between the two directions. This is surprising, because one would expect the time of flight to be the same when the water is still. However, when there is flow, there is also a phase difference,



Figure 17: Support structure printed to hold the transducers attached to the tube.

although smaller: for every different flux rate, the offset phase was subtracted from the measured $\Delta\phi$. The experiment was repeated several times and the same results were found. Different hypothesis were drawn to try to understand the phenomenon.

The first hypothesis was that imperfections of the relay board may lead to asymmetries of the phase propagation, but this assumption was ruled out by direct measurements at the switch terminals.

Another reason could be differences in the phase difference between TX and RX in the two transducers due to parameter tolerances.

- For higher velocities, the calculated phase decreases drastically with time. This makes it impossible to estimate the phase difference between the pulses in both directions. To understand this phenomenon, the pump was set at the maximum rate and it was set to measure for 20 minutes, sending a pulse every second in one direction, to better observe the absolute change in phase. The measured phase can be seen in Figure 19. It shows a fast decrease in phase for the first 200 seconds, and from second 500 starts to slowly increase. The main hypothesis for this is that, since PVC is extremely elastic, the pipe dilates and retracts due to the high velocity, taking into account that at the maximum rate, water moves at more than 50 cm/s and there is a strong pressure on the walls, which leads to uncontrolled dilatations. Moreover, this decrease and increase in phase is extremely noisy, and is due to strong vibrations in the tube that also produce a small change in the diameter and thus, in the time of flight. By touching the tube with the hand, these vibrations were felt with high velocities but not with low velocities, which confirms the hypothesis.

Taking into account these two aspects, it was decided to first explore the Doppler Effect method.

5.3.2 Measurements with Doppler Effect

The second attempt to measure the flow through the 24 mm tube consisted in clamping the transducers at the outside of the tube, as shown in Figure 20. To be able to measure

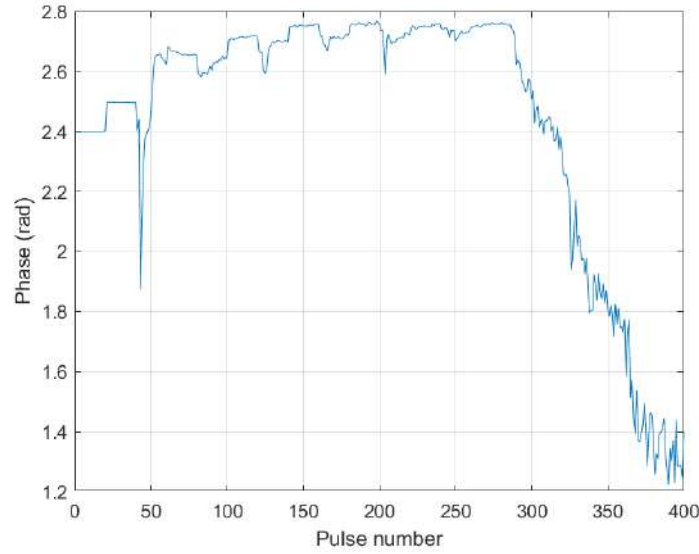


Figure 18: Phase of received pulses with increasing velocities from 0 to 8.8 l/min and switching every 20 pulses.

the frequency shift, the goal is to receive the signal which reflects from the heterogeneities of the fluid. In the case of tap water, the concentration of mineral salts is between 5 to 50 mg/L [20], which, as will be shown, is not enough for reflecting the signal. Thus, the only easily available element which can reflect the signal are air bubbles. With flowing water, the position of the RX transducer was moved until the reflected signal was best received. Taking into account the size of the tube, the maximum velocity is approximately 53 cm/s. Using the classic Doppler Ultrasound equation 22, the frequency shift should be 611 Hz. 6 different velocities were tested, and the Fourier Transform of the received signals are shown in Figure 21. It clearly shows that for higher velocities, the reflected signal on air bubbles is stronger, and thus the peak at the TX frequency, which is exactly 975 KHz is smaller. However, for smaller velocities, it can be observed how the air bubbles move toward the top of the tube and there is very little reflected signal. Thus, it shows that it is not possible to use Doppler Ultrasound with plain water, as it relies on the presence of significant heterogeneities in the liquid.

Nonetheless, the received signals can be processed to quantitatively assess the mean velocity. From Figure 21, it can be seen that the reflected signal is very broadband compared to the transmitted signal. To get an average value, the Power Spectral Density of the reflected signal is computed. To do so, only the frequencies of interest are taken, so that it does not contain the peak at 975 KHz. Then, the centroid of the PSD is computed, and that is considered to be the central frequency of the reflected signal [21]. It is calculated with the classical center of mass integrals

$$f_v = \frac{\int_{-0.5}^{0.5} x \cdot PSD(x) dx}{\int_{-0.5}^{0.5} PSD(x) dx} \quad (42)$$

where the frequencies have been normalized in the range from -0.5 to 0.5. With this, an

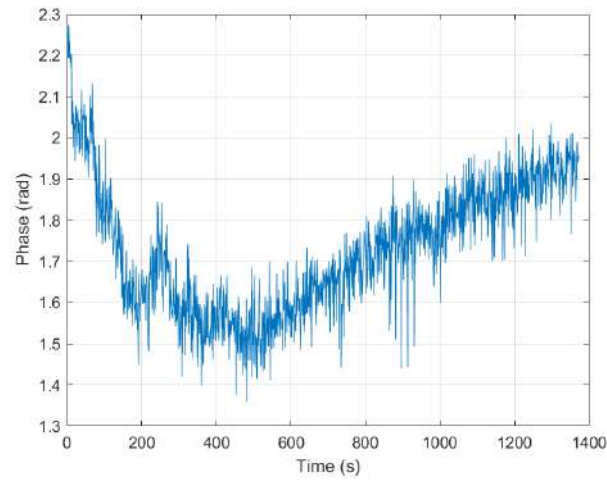


Figure 19: Phase change of received pulse during 20 minutes.



Figure 20: Set-up of transducers to detect reflections.

estimation of the mean frequency can be calculated, and thus the velocity and the flow as well. Figure 22 shows the comparison between the real flow and the estimated flow using the centroid of the PSD. From this section, we can conclude that with Doppler Ultrasound it is possible to estimate the flow of water but only when there are particles that can properly reflect the transmitted signal.

5.4 Velocity measurements in phantom: circular tube

In the first place, a system with a 40 mm PVC tube was assembled. However, there were turbulences due to abrupt changes in diameter. For this reason, we decided to use directly the perfusion phantom. As has been stated earlier, the goal is to measure the velocity inside the pipe located inside the phantom. At first sight, we can see that the tube is in contact, on its upper part, with the glass cover. Thus, it should be possible, although

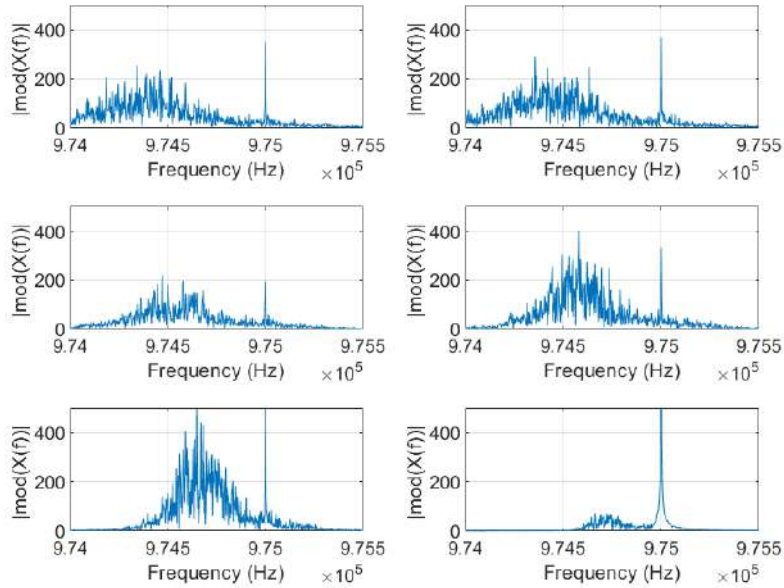


Figure 21: Fourier transform of the received signal for flows of 8.8, 8.1, 7, 5.5, 4 and 3 l/min, from left to right and top to bottom, respectively.

with an important signal loss, to send the ultrasonic beam through the glass, then a part a part of the power can transmit to the inside the tube, reflect at the bottom and go back to the upper surface by crossing the two media again. A support structure to hold the transducers to a flat surface with an angle α with respect to the surface was designed and printed with the same 3D printer. They were placed on the crystal at the last part of the tube, where we would expect the flow to be more laminar. After some adjustments to receive properly the reflection, measurements with flow were taken. The set-up can be seen in Figure 23. The following sequence was applied: for every pump flow rate, 2 pulses were sent in one direction; then, the output of the GPIO are inverted and thus 2 more pulses are sent in the opposite direction. To get an average, this was repeated 10 times. In total, for each flow value, 40 pulses were sent. The flow at the pump was increased from 0 to 8.5 l/min with steps of 0.5 l/min. Unfortunately, the results were not the desired. We can see in Figure 24 that for low velocities, the phase difference is almost zero, which means that there is very little flow. For higher values, it does change but without following any particular trend, as we would expect, and even decreases and has negative values. The same measurement was repeated several times, and the results were consistent. Again, we needed to find an explanation for the unsuccessful results. We expected constant phase difference for each pump rate, but this was not the case.

Fortunately, other researchers of the group were carrying out flow measurements with the same phantom in the MRI scanner, using the same pump at its maximum power (8.8 l/min). In some of the images, it was visible that there was water flowing between the tube and the glass cover. Figure 25 is a reconstruction from phase contrast measurements [22], looking from one side of the phantom. One can see that there is water in between

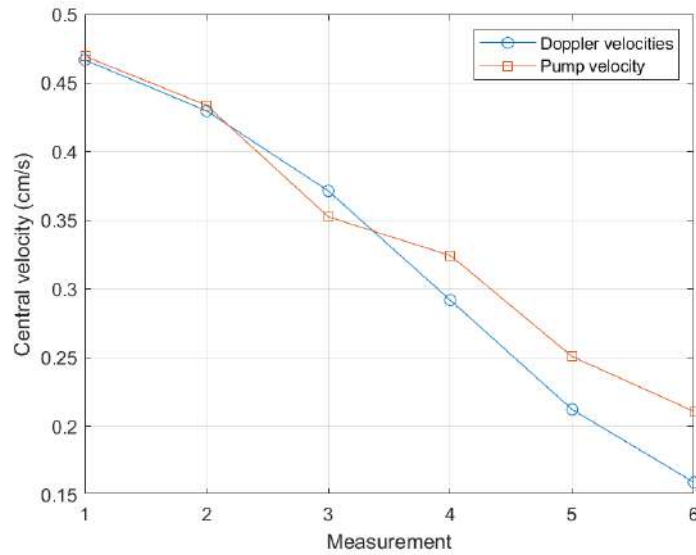


Figure 22: Comparison between real flow values and estimated.

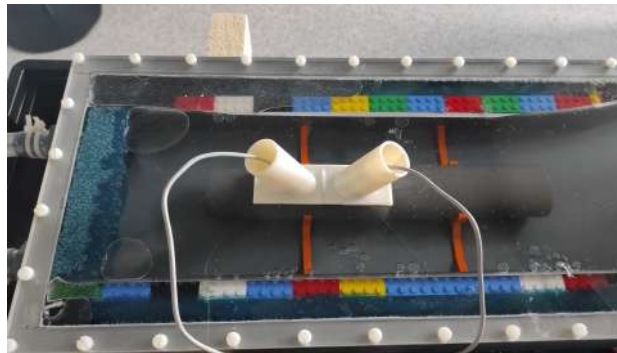


Figure 23: Transducers placed on top of the glass above the tube.

the top of the tube and the cover, and that is because the pressure of the phantom moves up the cover and allows water to flow in that region.

Hence, what we were measuring were mostly the reflections in the water between the glass and the tube, and since this layer is very thin (a few millimeters), one cannot expect a laminar flow. Furthermore, for high velocities, we also expect turbulence, and when this happens, there can be many unwanted reflections that can interfere in the path of the main wave.

5.5 Velocity measurements in phantom: rectangular cross-section

Again, the problem was in the device under test and not the flow-meter itself. The only option left was to place the transducers in a region of the phantom where the wave can travel freely and has a clean reflection at the bottom. Alternatively, one could also place one of the transducers in the bottom side of the phantom and measure the signal

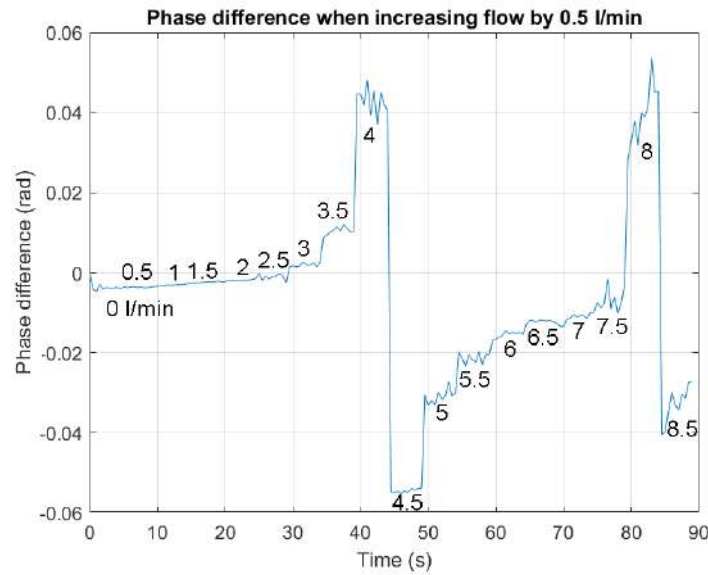


Figure 24: Phase difference of the upstream and downstream pulses with the transducers placed on the tube when increasing the flow at the pump by 0.5 l/min.

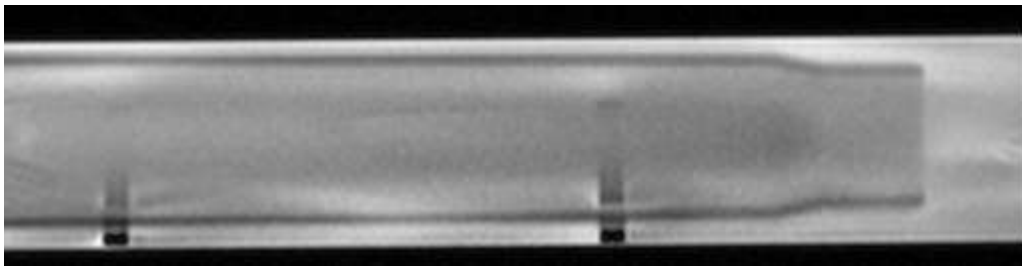


Figure 25: Image of the perfusion phantom taken with the MRI scanner using Phase Contrast MRI. [22]

transmitting directly through all the layers. If the signal is capable of transmitting through the PVC layer of 1 cm, this has the advantage that avoids one reflection and has less attenuation in water. On the other hand, the time of flight is reduced by half, hence a factor of 2 in resolution is lost. The first measurement consisted in repeating the sequence described earlier, with a flux increase of 0.5 l/min. The results are shown in Figure 26. Once again, the phase difference between the pulses in both directions does not increase linearly with the flux read at the pump. As can be seen, at the first velocity values it does increase, although not linearly, but at the change from 2 to 2.5 l/min it decreases by 0.05 rad, and in the next flux change it even goes down to negative values, and then back up again.

To further investigate the reason, Pulses were sent every 0.5 seconds and the pump speed was increased with the smallest possible resolution (0.1 l/min), to see how both the absolute phase of the received signal and the differential phase changes with speed. Only by looking at the absolute phase of Figure 27, the results are surprising. Poiseuille's Law

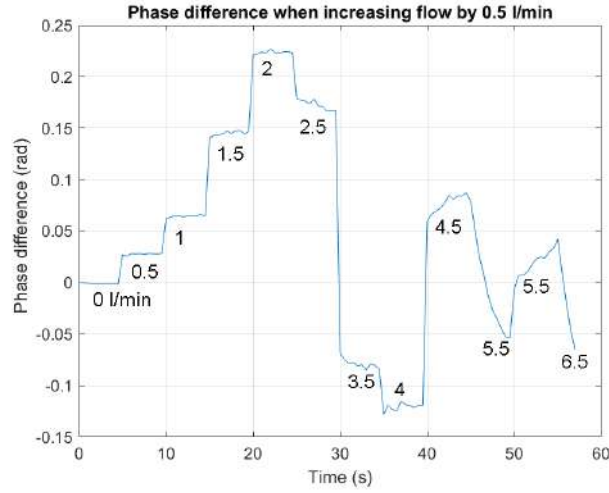


Figure 26: Phase difference between upstream and downstream pulses when increasing flow by 0.5 l/min repeatedly.

states that when there is a laminar flow, the pressure increases linearly with flow, and considering the elasticity of the cover and Hooke's law for small deviations, we expect the glass cover to increase in height linearly with flow. However, in Figure 27 can be seen that the phase does not increase linearly, but even the slope oscillates around a certain value from 3 l/min and above.

Moreover, when looking at the phase difference, it shows an increase, although non-linear, until the flux of 6 l/min, where there is a local maximum, and a local minimum at 7 l/min. The curve does not follow exactly the same pattern as Figure 26, which should be the same but with different sampling flow, and it is because were taken taken at different days and a slight different position of the transducer caused the travelling paths to be different.

However, we was observed that when pushing down the glass while keeping the flow constant, the amplitude of the received signal varied; this is a clear indicator that there might be interference between different waves inside the phantom and depending on the length of the path they add constructively or destructively. Moreover, it might produce unwanted changes in the measured phase. For this reason, it was decided to study this phenomenon and take into consideration that the received signal might be a superposition of different waves with different phases coming from the reflections due to a broad directivity of the acoustic beam.

5.5.1 Superposition of ultrasonic waves

To study the behaviour of the phase of the received pulses in the phantom, we need to simulate the different reflections and the change in height of the water channel. Recalling equation 1, the attenuation decays exponentially with distance, frequency and the attenuation coefficient. k_w , k_g , k_{PVC} , H_w , H_g and H_{PVC} are the attenuation coefficients and heights of the three different media involved: water, glass and PVC, respectively. The

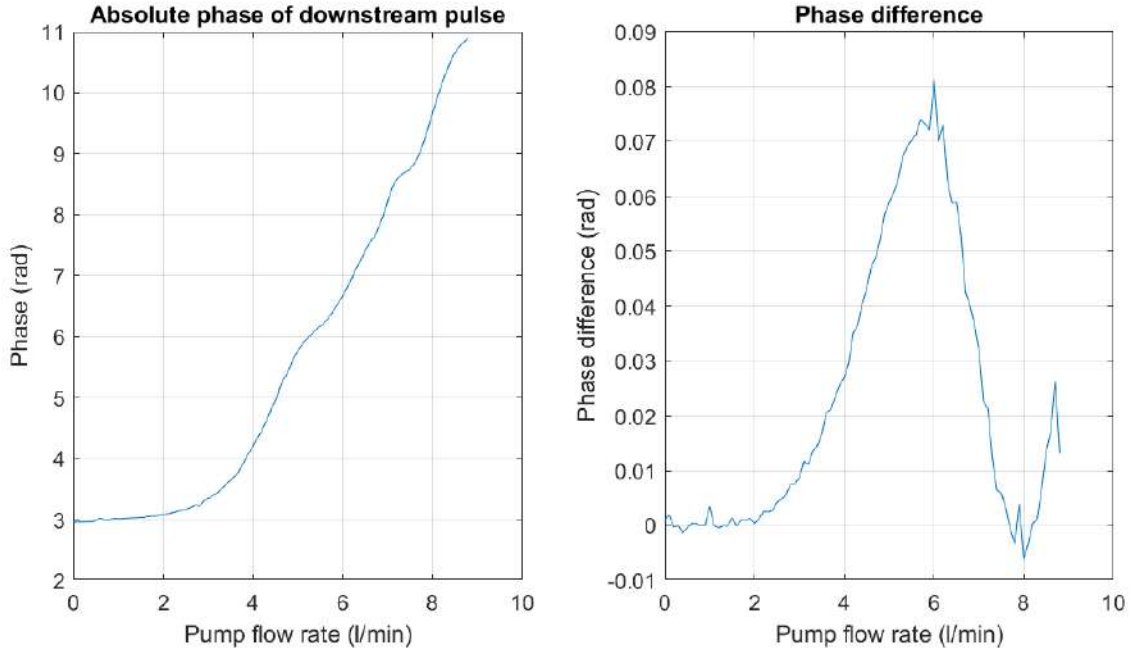


Figure 27: Phase of downstream pulse with the transducers set in direct transmission (left) and phase difference between upstream and downstream (right).

grease is not considered, as we assume that all waves entering the grease are received by the transducer and the attenuation is the same in all the cases. Some of the reflections are depicted in Figure 28.

Moreover, all the angles are different because the distance between the two transducers is fixed, and the angles at each medium interface must obey Snell's Law of refraction. For this reason, in each medium the angles are different, and will be denoted as α , β and γ , which can be seen in Figure 29 for two different paths.

To make this model more generic, we could consider reflections in all the layers, including the glass and the PVC. However, the change in velocity of propagation due to different flow velocity only applies to water, and the height change also only affects the water. Thus, having a superposition of waves with different paths in the glass or PVC, but no reflections in water would only add an almost constant phase value in all the different situations. It would not be identical because the angle β_n would be different. However, the difference should be neglected.

Because the angles α_i depend on the properties and geometry of the two other media, in this case they should be considered for calculating the refraction angles and reflection coefficients. We will denote n as the index referring to each different path. For instance, in Figure 29, the case in which there are no reflections, the index is $n = 0$; when there are 2 reflections, which is the second path, $n = 1$, and so on. The maximum number of paths can be truncated at N , being the maximum index n that we consider. The ultrasonic

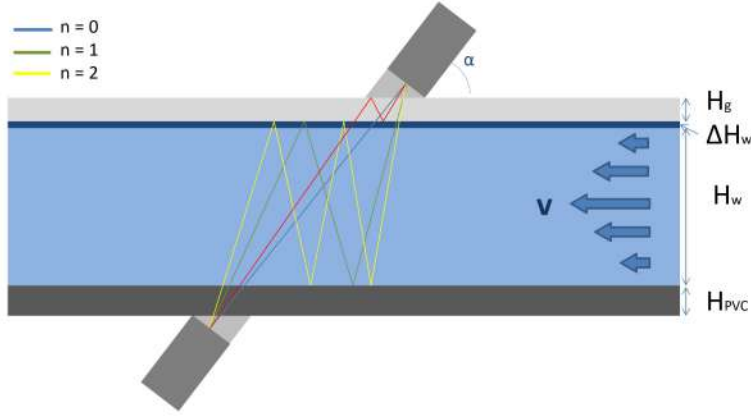


Figure 28: Some of the possible reflections inside the phantom.

signal at the receiving transducer for each different index will be:

$$s_n(t) = A_n \cos(2\pi f t + \phi_n) e^{-H_g k_g f / \sin \alpha_n} \quad (43)$$

$$e^{-(2n+1)H_w k_w f / \sin \beta_n} \cdot e^{-H_{PVC} k_{PVC} f / \sin \gamma_n} \quad (44)$$

For the Reflection coefficients between two medium for acoustic waves, we could use the formula from [23]. However, since we only want to find a qualitative result and taking into account the angle will only change slightly the result, the formula for normal incidence will be used. R_{PVC} is the reflection coefficient between water and the PVC bottom, and R_g , between water and the acrylic glass. Thus:

$$A_n = (R_{PVC} \cdot R_g)^n \quad (45)$$

The values of ϕ_n are given by the amount of reflections and speed of sound of each medium, which can be found in Table 1.

$$\phi_n = \text{constant} + 2\pi f \cdot (H_g / \sin \alpha_n + (2n + 1)H_w / \sin \beta_n + H_{PVC} / \sin \gamma_n) \quad (46)$$

with $0 \leq n \leq N$. Considering the principle of superposition, the measured signal will be:

$$s(t) = \sum_{n=0}^N s_n(t) \quad (47)$$

And the only thing missing is to calculate the angles α_n , β_n and γ_n . According to Snell's Law, the relation between incident and transmitted angles between medium a and medium b is:

$$\frac{\sin \theta_a}{c_a} = \frac{\sin \theta_b}{c_b} \quad (48)$$

where θ_a and θ_b are the angles with respect to normal incidence and c_a and c_b the propagation velocities of sound in each medium. Thus, if we use the angle of the transducer with respect to the medium interface α , the equation writes:

$$\frac{\cos \alpha_a}{c_a} = \frac{\cos \alpha_b}{c_b} \quad (49)$$

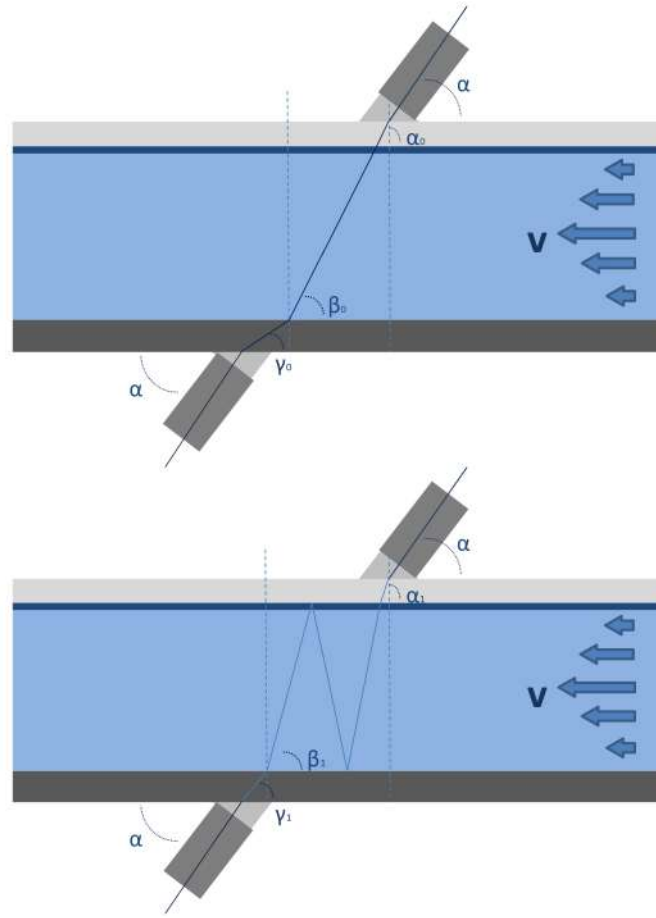


Figure 29: Description and definition of angles in the case in which there are no reflections ($n = 0$) (top) and when there are 2 reflections ($n = 1$) (bottom)

Thus, in each medium, the refracted angle will be given only by the propagation speed in that medium and in the first medium. Propagation velocities in grease, glass, water and PVC are c_0, c_1, c_2 and c_3 , respectively. α is the angle of emission from the transducer, and α_n, β_n and γ_n are the angles at each different medium for each different index n .

$$\cos \alpha_n = \frac{c_1}{c_0} \cos \alpha \quad (50)$$

$$\cos \beta_n = \frac{c_2}{c_1} \cos \alpha_n = \frac{c_2}{c_1} \frac{c_1}{c_0} \cos \alpha = \frac{c_2}{c_0} \cos \alpha \quad (51)$$

$$\cos \gamma_n = \frac{c_3}{c_0} \cos \alpha \quad (52)$$

Since the last medium is grease, like the first medium, the last angle is the same as the first.

The horizontal distance between the two transducers, to receive the main signal can be calculated by equation 53.

$$d = \cot \alpha_0 H_g + \cot \beta_0 H_w + \cot \gamma_0 H_{PVC} =$$

$$= \frac{\cos \alpha}{c_0} \left(\frac{c_1 H_g}{\sqrt{1 - (\frac{c_1}{c_0} \cos \alpha)^2}} + \frac{c_2 H_w}{\sqrt{1 - (\frac{c_2}{c_0} \cos \alpha)^2}} + \frac{c_3 H_{PVC}}{\sqrt{1 - (\frac{c_3}{c_0} \cos \alpha)^2}} \right) \quad (53)$$

Substituting all the values, and with an angle $\alpha = 60^\circ$, we obtain a distance of $d = 7.1 \text{ cm}$. With this, all the output angles of all the possible reflections can be computed by adding in the middle term of equation 53 the number of times the signal travels the vertical direction H_w :

$$d(\alpha) = \frac{\cos \alpha}{c_0} \left(\frac{c_1 H_g}{\sqrt{1 - (\frac{c_1}{c_0} \cos \alpha)^2}} + \frac{c_2 (2n - 1) H_w}{\sqrt{1 - (\frac{c_2}{c_0} \cos \alpha)^2}} + \frac{c_3 H_{PVC}}{\sqrt{1 - (\frac{c_3}{c_0} \cos \alpha)^2}} \right) \quad (54)$$

Since d is fixed, we can find the angle α which satisfies the previous equation for each different index n , and it is done numerically, as equation 54 is transcendental. Figure 30 show angles α for each different n . This discret set of angles are the theoretical angles in which there can be reflections in water, although the transducer cannot emit in all of them. The following simulation consists in supposing that the change of the height H_w

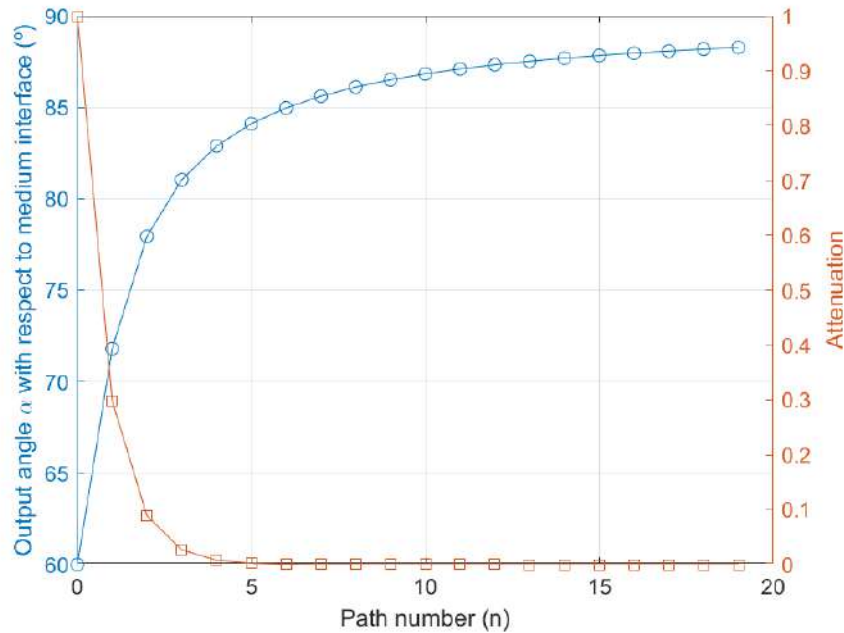


Figure 30: Output angles from the TX transducer to reach the RX transducer with $2 \cdot n$ reflections (left axis), attenuation due to reflections and longer path (right axis)

is linear with flow velocity. The superposition of all the different waves has been applied

for each different velocity, in the range between 0 and 1 cm/s. It has been done in two different cases by changing the sign of the added velocity: $c'_2 = c_2 \pm v$. Then, when all the signals are computed and summed, we have applied the same phase estimation algorithm as in the measurements, using an arbitrary sinusoidal signal as reference. The simulation has been done with 5000 steps of $2 \cdot 10^{-4}$ cm/s, and truncated at the index $n = 5$ for two reasons, depicted in Figure 30.

- The output angle of the transducer gets far off from the central angle, which reduces the amplitude of emission.
- The decay in amplitude due to two extra reflections in each path and media attenuation causes the signal to be negligible from $n = 5$.

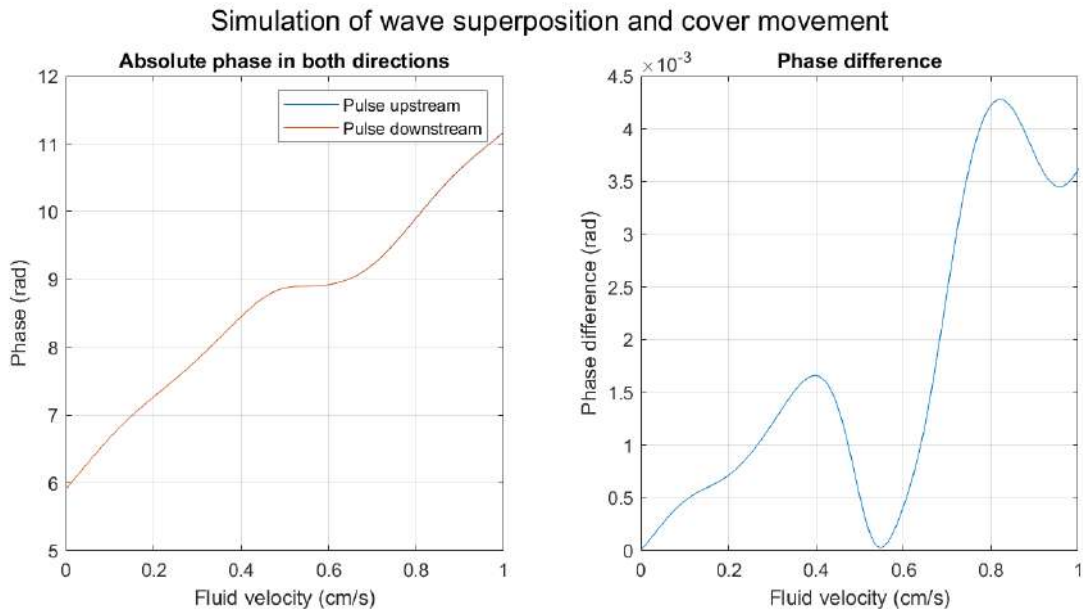


Figure 31: Simulated absolute phase of upstream and downstream pulses (left) and their difference (right).

The results of the simulation are shown in Figure 31. The difference of phase by subtracting the two phases is also shown. A linear increase of the water height leads to, if there are multiple waves superposed, a non-linear increase in phase. In the plot where the absolute phases are shown, their difference is so small compared to the absolute value, that the two lines don't differ.

It is important to understand that this model only tries to obtain qualitative results. The attenuation coefficients, propagation velocity and acoustic impedance are taken from the references, and it is impossible to know their exact values. Although these results only resemble qualitatively the ones obtained experimentally in Figure 27, the simulation suggests that multiple reflections can have an effect on the measured phase, by showing a maximum and minimum in the $\Delta\phi$ curve. Thus, the phase of the received signal is not proportional to the path travelled along the water, and the difference in phase is not linear

with speed. Thus, it is an indication that in the phantom there are multiple reflections which affect the phase of the measured signal.

Thus, according to such a model, the multiple reflections not only produce artifacts on the phase vs height curve, but also in the phase difference when the water flows in different directions. This means that if in the receiving transducer there is a superposition of waves which have travelled different paths, the fact that for each velocity these paths have been different, causes the phase measurement of received wave to vary non-linearly with the propagation velocity.

On the one hand, one can also simulate the behaviour when there is a linear increase of height, proportional to velocity, but without considering reflections ($N = 0$). On the other hand, we can also simulate that there are reflections but no change in water height.

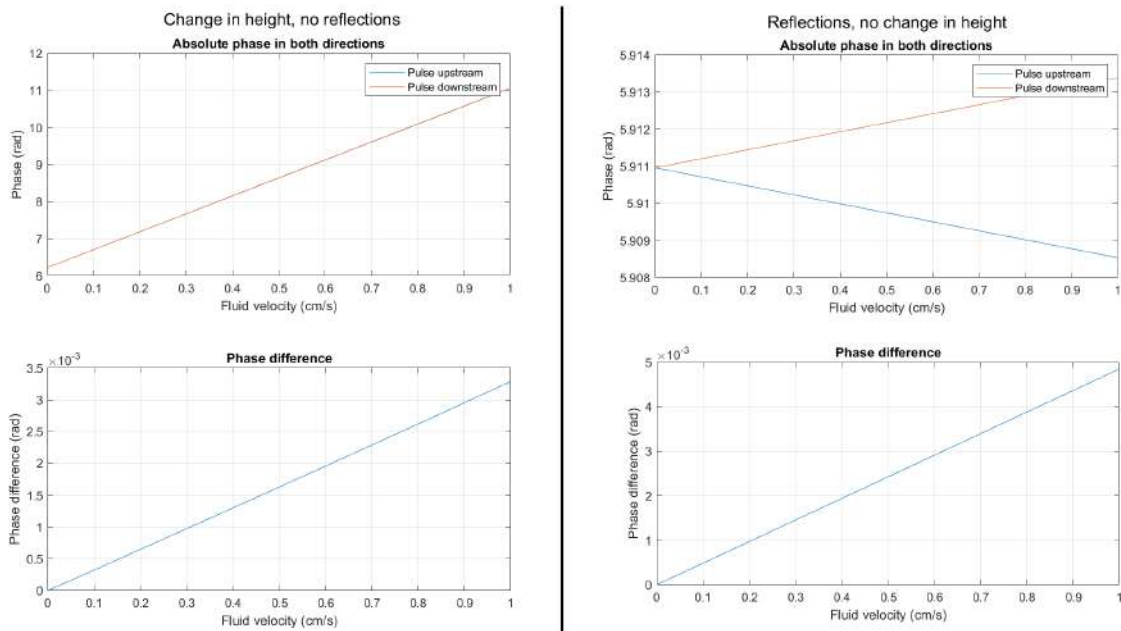


Figure 32: Simulated phases in the two cases: height change but no reflections considered (left), reflections considered ($N = 5$) but no change in height (right).

Both cases in Figure 32 show a linear increase of the phase difference as a function of fluid velocity.

In the case on the left, it shows that even with a change in height of the water path, if there are no superposition of waves with different phases, the phase difference is linear. This is to be expected, as it is the theoretical case with just a slightly different phase in both directions.

However, in the case of reflections but without height change, the $\Delta\phi$ is surprisingly linear though all reflections have travelled a different path. However, in all the velocities the paths have been the same, hence the change in phase is linear.

From the measurements and simulation, we formulate the following hypothesis:

1. In the receiving transducer we are not only receiving the main wave but also multiple reflections created in the different medium interfaces. If the cover does not move, the paths of all the reflections are constant and if the only difference when changing the fluid velocity is the wave's propagation speed, the $\Delta\phi$ should be proportional to the velocity.
2. If there is a movement in the cover glass due to the change in velocity, this should not affect the linearity as long as there are no reflections.
3. If both reflections and movement occur, then the non-linearities appear and invalidate the ΔToF method.

In the current set-up, we have both artifacts. In theory, by fixing one of the two, the linearity should be achieved.

The most interesting step would be to be able to measure only the direct signal, not only for the purpose of this thesis but in case this phase sensor needs to be used for another project.

Several possibilities arise to reduce the interferences.

5.5.1.1 Adaptive filter One solution would be to use a third transducer and place it in a location where it can receive a significant amount of reflections, but not the signal of interest, which is only the one which we want to measure with the receiving transducer. If this could be achieved, then, according to the diagram in Figure 33, the input signal

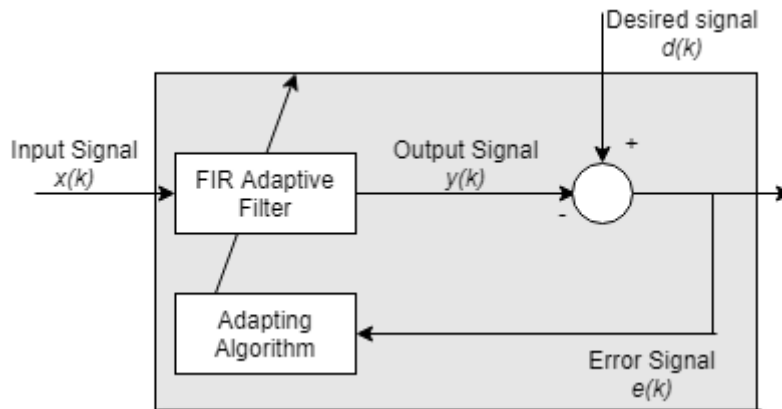


Figure 33: Block diagram of an adaptive filter.

$x(k)$ would be the signal measured in transducers 1 and 2, which is the one used in all the measurements until this point, and $d(k)$ would be the signal from the 3rd transducer. Thus, the error signal $e(k)$ would contain only the clean signal without any interference.

However, its implementation is not trivial. The Red Pitaya contains only 2 ADCs, and both are already in use. A second board would be needed in parallel, with the ADCs using the same clock signal, and they should be controlled with two different laptops and software running in parallel. Another option would be to use the option to control

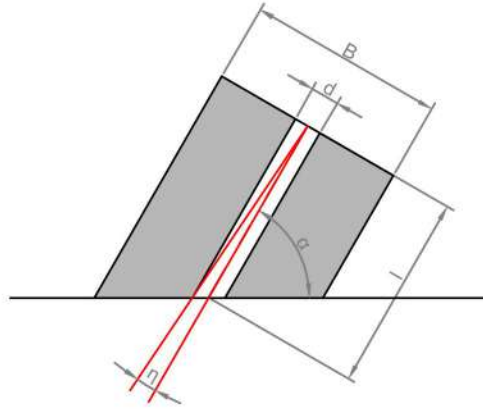


Figure 34: Blueprint of the collimator

two Red Pitayas in parallel, such as STEMLab 125-14 X-Channel System, which requires a synchronization cable and a specific software to control several Red Pitaya Boards in parallel. However, in principle the software to run this multi-CPU system is different than the server-client software used in this project, and would need to be merged, which is not a trivial task. Thus, this is a possibility to solve the interference issue, but has not been tried due to the lack of time and difficulty.

5.5.1.2 Acoustic beam collimator The second option is to build a device able to focus the beam leaving and entering the transducers. There are many different ways of doing so: [24] uses a cone-shape tube in order to focus the beam at an exact position, where the geometrical focus is found. [25] uses acoustic surface waves with a two-dimensional array of sub-wavelength holes to improve the directivity of the transducer. However, these solutions would require a lot of time, and we had no guaranty that would solve the problem. An easier way to do so is by using a highly absorbent material, such as polystyrene or polystyrene foam, which have rough surfaces. The idea is to drill a hole, fill it with the coupling grease, and put it between each transducer and the surface. The semi-aperture angle of the collimator is given by its length, diameter and the incidence angle α . The blueprint can be seen in Figure 34. Distance B is the side of the prism and does not affect the geometry of the aperture. All the collimators have been built with a size $B = 30mm$.

$$\tan \eta = \frac{d/2}{l - d/2 \cot \alpha} \quad (55)$$

Before building a collimator, it is important to calculate, with the different reflections, which is the maximum angle we can make to filter all the beams except for the direct path. With $\alpha = 60^\circ$, the path with the most similar entrance angle is when there are 2 reflections in water, and the angle is 4.1° . The semi-aperture angle η must be smaller than the incidence angle of the first reflection. The wider is the aperture, the less directive is the beam, but also the more power goes through. On the other hand, the longer the hole, the longer is the path and the signal attenuates exponentially with distance. If the

attenuation coefficient is unknown, an analytic optimization is difficult and thus we opted for a trial/error approach. With a hole of 5 mm in diameter, we would need the collimator to be 40 mm long, making an angle of 3.5° . One of the collimators is shown in Figure 35. Again, a 3D structure was designed and printed to place the collimators and transducers firmly on the flat surfaces.



Figure 35: 5° collimator built.

5.6 Velocity measurements in the tube inside the phantom with collimator

The transducers with collimators were placed in the phantom in the same way as in the previous measurements. They were placed at the distance where in theory the main beam should arrive for the given angle of $\alpha = 60^\circ$ and adjusted by trial and error until the right spot was found. It was observed that with the collimators, only 10% of the signal went through, compared to the case without.

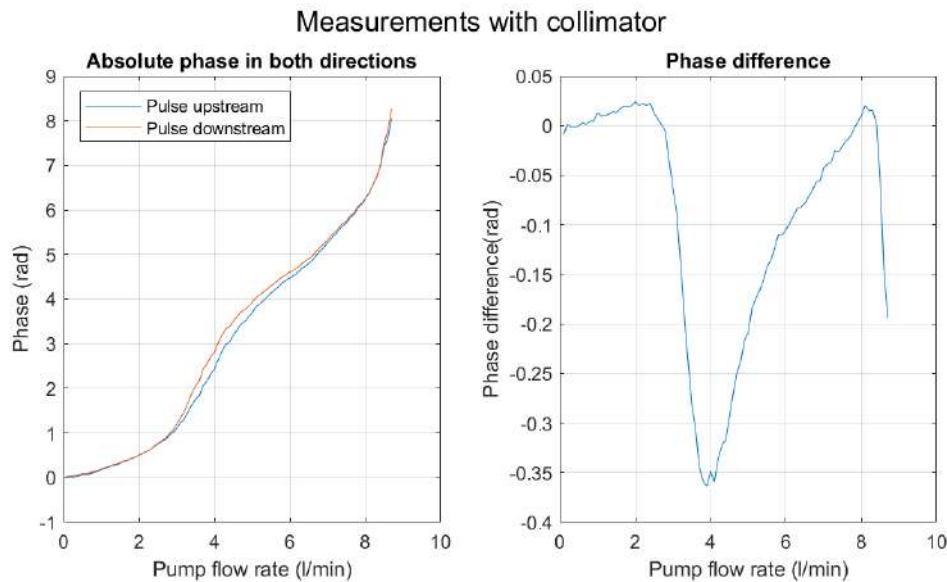


Figure 36: Absolute phase of the pulses in both directions when a 3.5° collimator is used(left) and their difference (right).

Figure 36 on the left shows the phase of the pulses in both directions of the flow. As can be seen, and, unlike in the case without collimator in Figure 27, the phase shows less

ripples by using the collimator to cancel the measuring of reflections. Moreover, if we plot the phase difference as a function of the pump flux, as the right plot on Figure 36 shows, we can see that in the lower velocities, up to 2.5 l/min, the difference is approximately linear. From there, there is a fast decrease until the curve hits a minimum at 4 l/min and then increases again until 8 l/min. By comparing the two figures, we can see that the less linear the absolute phase is, the less linear their difference is.

We have seen a change with respect to the case without collimator, but it seems as the interferences are not completely filtered out and hence still compromise the linearity. and thus cannot find the linearity. The most possible explanation is that inside the collimator, the interface between the grease and the polystyrene is not 100% absorbent and some of the wave reflections can arrive at the receiving transducer. Together with the height change, still make the ΔToF measurements invalid.

Thus, the only option left is to try to minimize the movement of the acrylic crystal. It was observed, surprisingly, that the cover, without any pressure applied, was concave, and when working at the maximum flow, it flattened more than 1 mm, as can be seen in Figure 37.

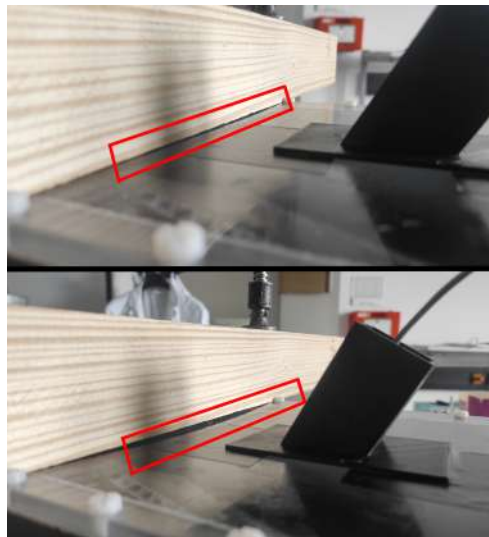


Figure 37: Difference in concavity in 8.8 l/min (top) and 0 l/min (bottom).

In order to prevent this movement, a clamping structure was assembled on the phantom with wood and two clamps.

5.7 Velocity measurements in the tube inside the phantom with collimator and clamping structure

For the measurements, the transducers were kept in the same position with the collimators, and the clamping structure shown in Figure 38. As Figure 39 shows, the results improve. Although in the absolute phase it is not flat, as we would expect if there were no movement, and there is a local maximum, the increase in phase due to movement is 30

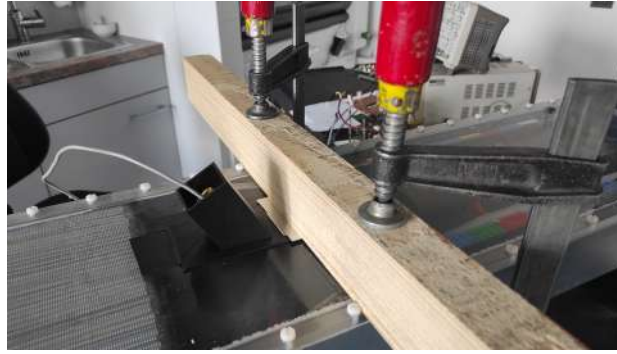


Figure 38: Clamping structure to prevent the movement of the acrylic glass.

times smaller than in Figure 36, as expected from the physics. This shows that the clamping structure has helped in reducing the movement but not yet completely. Nonetheless, when subtracting the two phases, we obtain a monotonically increasing curve, which is at least piece-wise linear with flow. The phase when the flux is close to the maximum of the pump is not shown, as in that region the movement of the cover was still too big, thus invalidating the data. However, when using equation 20 to calculate v_m from $\Delta\phi$, the obtained v_m is by more than 50 times as high as expected, even though the linearity is correct. Thus, it is needed to scale down the result.

More measurements were taken by calculating the $\Delta\phi$ 10 times for each different flow rate, increasing from 0 to 6 l/min with steps of 0.5 l/min. Moreover, the same experiment was repeated by placing the phantom inside the MRI scanner *Siemens Magnetom Vita 3T* by repeating MRI sequences for the same values of the pump flow. Velocities were taken by using the phase-contrast technique [22] with Velocity Encoding (VENC). This procedure was carried out with the help of MRI experts of the Institute of Biomedical Imaging.

With these results, we can take an average for each flow level from Figure 40 and compute a linear regression to obtain the average slope. With the velocity results from the scanner measurements, a linear regression has also been computed. We have defined a calibrating factor K :

$$K = \frac{\text{slope of ultrasound}}{\text{slope of MRI}} \quad (56)$$

To calibrate the velocities of the Ultrasound measurements, they are divided by K . The results as shown in Figure 41.

There are still considerable deviations from the desired linearity, but we have to consider that the experimental situation is still sub-optimal. The acrylic glass has a big tension on its perimeter due to the tightly attached screws, and so it causes a big concavity due to its elasticity. Regardless of this, the r^2 factor of the linear regression of the US data is 0.9697.

Moreover, the pump does not seem to have valid flow readings for lower velocities, and for this reason it is hard to tell if the change of slope is caused by invalid readings or if

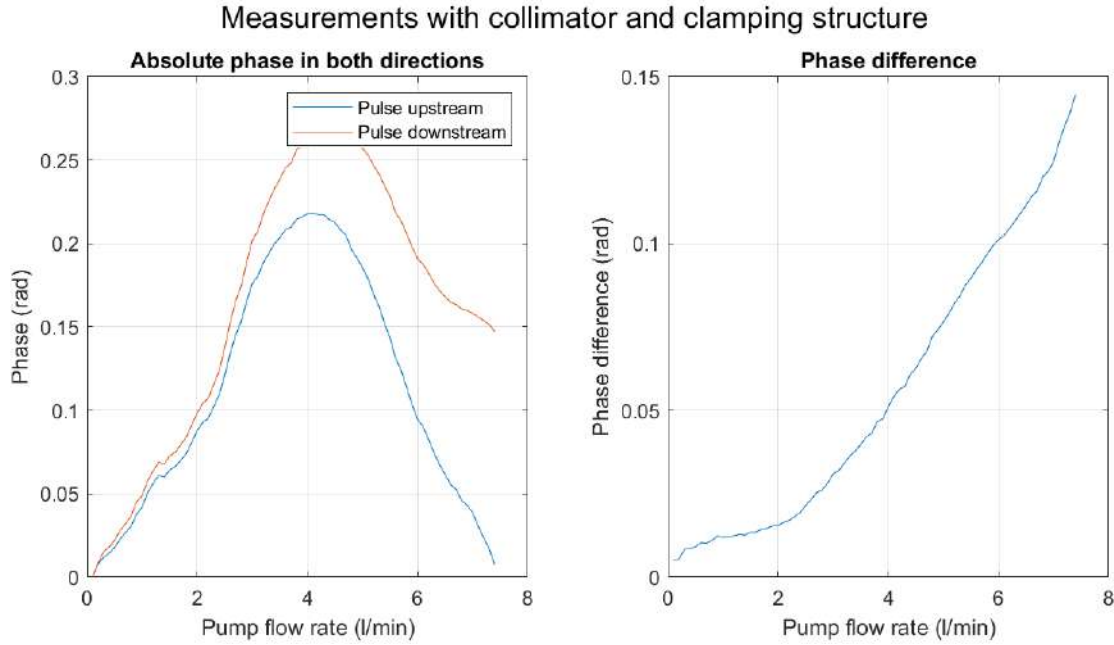


Figure 39: Measurements after adding clamping device to prevent movement. Absolute phases (left) and differential phases (right).

there are still uncontrolled changes of the cover movements.

The pump has two modes of operation: with revolutions per minute (rpm) and by flux (l/min). All the measurements have been done reading the value of flux. However, one value of l/min can be different values of rpm because its resolution is only 0.1 l/min, and thus produce fluxes. Hence, repeatability is a big issue with this pump, and thus an alternative flow-meter should be used in parallel to the Ultrasonic Δ ToF sensor for calibrating purposes. It should be placed right before or after the pump to disturb as little as possible the flow. At the moment, there is no such reference device available, so this is left as a future work.

The variance of the measured phase for different velocities was measured by sending 2 pulses in each direction and then repeating 100 times. A maximum standard deviation of 0.03 radians has been found, which is equivalent to less than 0.05 cm/s after the calibration.

6 Conclusions and future work

A non-invasive Ultrasound flow-meter has been developed to measure local velocities in a perfusion phantom. The Δ ToF method has been implemented by means of a phase estimation algorithm to detect the time difference. Due to certain interfering effects, the obtained flow data deviate from the theoretically expected ones and hence a calibration is required. Unexpected mechanical deformations of the plexiglass cover of the used flow phantom introduced complications during the measurements.

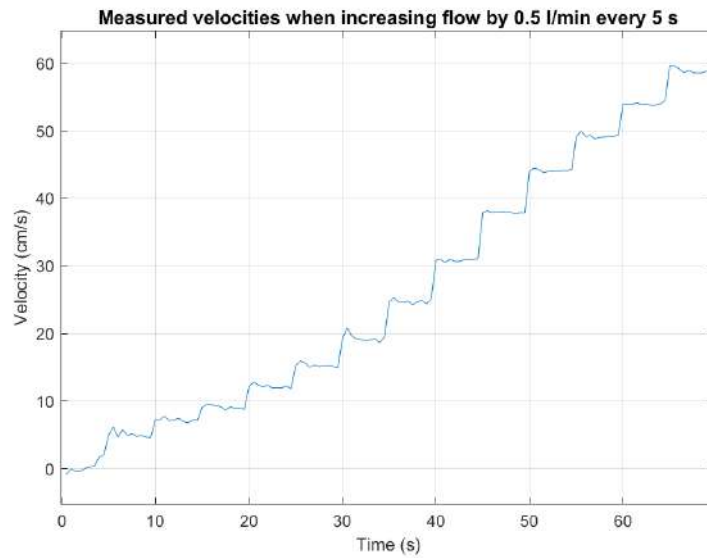


Figure 40: Measures taken with increasing the flux read at the pump every 5 seconds and changing with steps of 0.5 l/min.

A prototype has been designed, built and tested. for further progress the deformation problem in the phantom needs to be tackled. Due to the current limitations of the setup, the obtained results must be considered as provisional. However, all important mechanisms and sources of artifacts have been identified and described, so that important issues for a re-design are now known.

The currently used signal generation and acquisition unit is fully operative but needs some mechanical re-design for making the instrumentation compact and reliable. With respect to the software, it successfully implements the communication with the digital hardware and is able to carry out the sequences that have been used for the measurements. However, optimization is still required, and the calibration phase should also be added to the software, as for now it is done in a separate Matlab script.

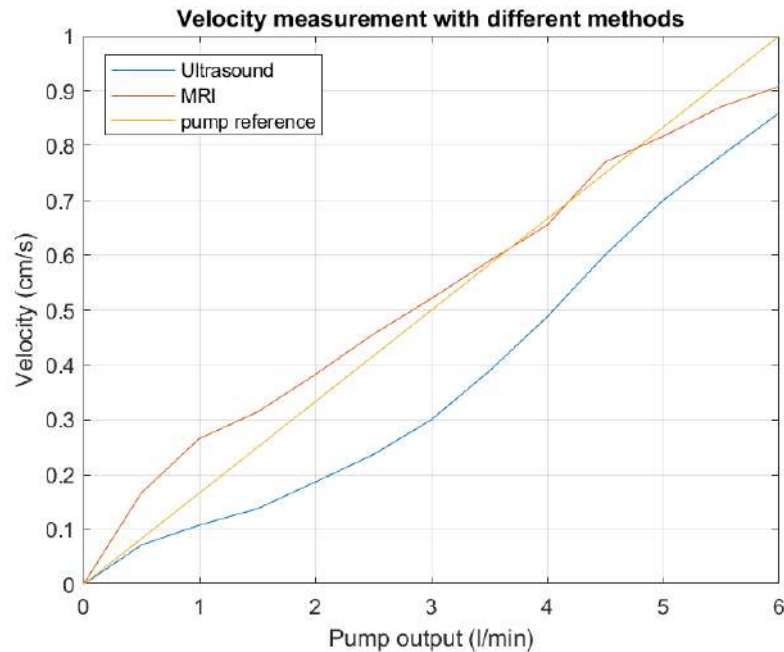


Figure 41: Comparison of velocity values after calibration with MRI.

References

- [1] A. Adler, “Simulation of magnetization in flows in magnetic resonance imaging”, e Institute of Diagnostic and Interventional Radiology Göttingen, Jan. 2021.
- [2] M. Anklin, W. Drahm, and A. Rieder, “Coriolis mass flowmeters: Overview of the current state of the art and latest research”, *Flow Measurement and Instrumentation*, vol. 17, pp. 317–323, 6 Dec. 2006, ISSN: 09555986. DOI: 10.1016/j.flowmeasinst.2006.07.004.
- [3] H. Takahashi, N. M. Dung, K. Matsumoto, and I. Shimoyama, “Differential pressure sensor using a piezoresistive cantilever”, *Journal of Micromechanics and Microengineering*, vol. 22, p. 055015, 5 May 2012, ISSN: 0960-1317. DOI: 10.1088/0960-1317/22/5/055015.
- [4] A. Venugopal, A. Agrawal, and S. Prabhu, “Review on vortex flowmeter—designer perspective”, *Sensors and Actuators A: Physical*, vol. 170, pp. 8–23, 1-2 Nov. 2011, ISSN: 09244247. DOI: 10.1016/j.sna.2011.05.034.
- [5] E. Strangas and T. Scott, “Design of a magnetic flowmeter for conductive fluids”, *IEEE Transactions on Instrumentation and Measurement*, vol. 37, pp. 35–38, 1 Mar. 1988, ISSN: 00189456. DOI: 10.1109/19.2659.
- [6] J. Reyes, “Modeling and simulation of ultrasonic flow meters: State of art”, IEEE, Sep. 2010, pp. 1–7, ISBN: 978-1-4244-6740-2. DOI: 10.1109/ANDESCON.2010.5634018.

- [7] R. C. Baker, “Turbine flowmeters: Ii. theoretical and experimental published information”, *Flow Measurement and Instrumentation*, vol. 4, pp. 123–144, 3 Jan. 1993, ISSN: 09555986. DOI: 10.1016/0955-5986(93)90048-N.
- [8] X. J. Li and P. H. J. Chong, “Design and implementation of a self-powered smart water meter”, *Sensors*, vol. 19, p. 4177, 19 Sep. 2019, ISSN: 1424-8220. DOI: 10.3390/s19194177.
- [9] A. Selfridge, “Approximate material properties in isotropic materials”, *IEEE Transactions on Sonics and Ultrasonics*, vol. 32, pp. 381–394, 3 May 1985, ISSN: 0018-9537. DOI: 10.1109/T-SU.1985.31608.
- [10] Y. Takeda, *Ultrasonic Doppler Velocity Profiler for Fluid Flow*. Springer Japan, 2012, vol. 101, ISBN: 978-4-431-54025-0. DOI: 10.1007/978-4-431-54026-7.
- [11] P. Demin, *Pulsed nmr system*.
- [12] *Ultrasonic flow sensor transducer*, US0014-001, Audiowell International, 2015. [Online]. Available: https://audiowell-international.com/products/US0014-001%20Product%20Specification_2-2018.pdf.
- [13] *300mhz, low-power, high-output-current, differential line driver*, MAX4147, Maxim Integrated, 1997. [Online]. Available: <https://www.analog.com/media/en/technical-documentation/data-sheets/MAX4147.pdf>.
- [14] F. M. H.H. / Gundlach, *Taschenbuch der Hochfrequenztechnik*, 2nd ed. Springer Verlag, 1962.
- [15] *Ultralow distortion, ultralow noise op amp*, MAX333A, Analog Devices, 2008. [Online]. Available: <https://www.analog.com/media/en/technical-documentation/data-sheets/AD797.pdf>.
- [16] *Precision, quad, spdt, cmos analog switch*, MAX333A, Maxim Integrated, 1999. [Online]. Available: <https://www.analog.com/media/en/technical-documentation/data-sheets/MAX333.pdf>.
- [17] M. Steffes, “Noise analysis for high-speed op amps”, Texas Instruments, 1996.
- [18] T. Trimmal, “Pulsed sequence nuclear magnetic resonance spectrometer based on a red pitaya”, Institute of Biomedical Imaging, 2022.
- [19] S. Mileiko, O. Cetinkaya, A. Yakovlev, and D. Balsamo, “A non-intrusive ultrasonic sensor system for water flow rate measurement”, *IEEE*, Aug. 2021, pp. 1–6, ISBN: 978-1-7281-9431-8. DOI: 10.1109/SAS51076.2021.9530165.
- [20] A. Azoulay, P. Garzon, and M. J. Eisenberg, “Comparison of the mineral content of tap water and bottled waters.”, *Journal of general internal medicine*, vol. 16, pp. 168–75, 3 Mar. 2001, ISSN: 0884-8734. DOI: 10.1111/j.1525-1497.2001.04189.x.
- [21] “Fpga-based doppler frequency estimator for real-time velocimetry”, *Electronics*, vol. 9, p. 456, 3 Mar. 2020, ISSN: 2079-9292. DOI: 10.3390/electronics9030456.
- [22] D. T. Wymer, K. P. Patel, W. F. Burke, and V. K. Bhatia, “Phase-contrast mri: Physics, techniques, and clinical applications”, *RadioGraphics*, vol. 40, pp. 122–140, 1 Jan. 2020, ISSN: 0271-5333. DOI: 10.1148/rg.2020190039.

- [23] C. Mei, *Two dimensional waves*. 2004.
- [24] C. Huang, R. Haouari, H. Gao, V. Rochus, and X. Rottenberg, “A subject-specific acoustic collimator for multi-index ultrasound neuron modulation system”, IEEE, Oct. 2018, pp. 1–9, ISBN: 978-1-5386-3425-7. DOI: 10.1109/ULTSYM.2018.8580081.
- [25] J. Christensen, A. I. Fernandez-Dominguez, F. de Leon-Perez, L. Martin-Moreno, and F. J. Garcia-Vidal, “Collimation of sound assisted by acoustic surface waves”, *Nature Physics*, vol. 3, pp. 851–852, 12 Dec. 2007, ISSN: 1745-2473. DOI: 10.1038/nphys774.
- [26] Z. B. B.R., “Red pitaya schematics”, Red Pitaya, 2014.

Appendices

A Appendix: Manual

A.1 Hardware

1. Connect pin 0 (GND) of extension connector E1 to power supply ground.
2. Place T-junction at the DAC1. One output to *balun* input and the other to ADC2.
3. Connect Control 1 to pin 7 of Extension connector E1 and Control 2 to pin 9, as shown in Figure 42.
4. Connect the rest of the pins of the switch as shown in Figure 43
5. Connect the 4 boards to $\pm 5V$ power supply via the red, black and brown wires that end up in the 4 3-pin connectors.

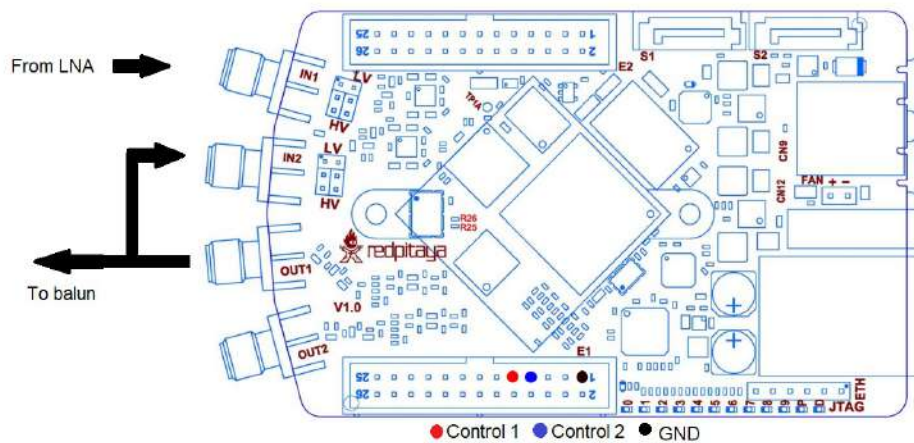


Figure 42: From Red Pitaya Schematics [26]

A.2 Software

All the codes can be found in the following GitHub repository:

<https://github.com/pasicl/Ultrasound-flowmeter>.

1. Download bootable alpine image from the Red Pitaya webpage.
2. Write the image to an empty SD card of at least 4 GB.
3. Connect via Ethernet cable the RP to a PC, and begin SSH connection. More detailed documentation can be found in <https://redpitaya.readthedocs.io/en/latest/>.
4. Via the host computer's command prompt, copy the files in the Server folder from the GitHub repository to the SD card
5. Load the *bitstream* file to write the FPGA:

```
1 cat pulsed_nmr.bit > /dev/xdevcfg
```

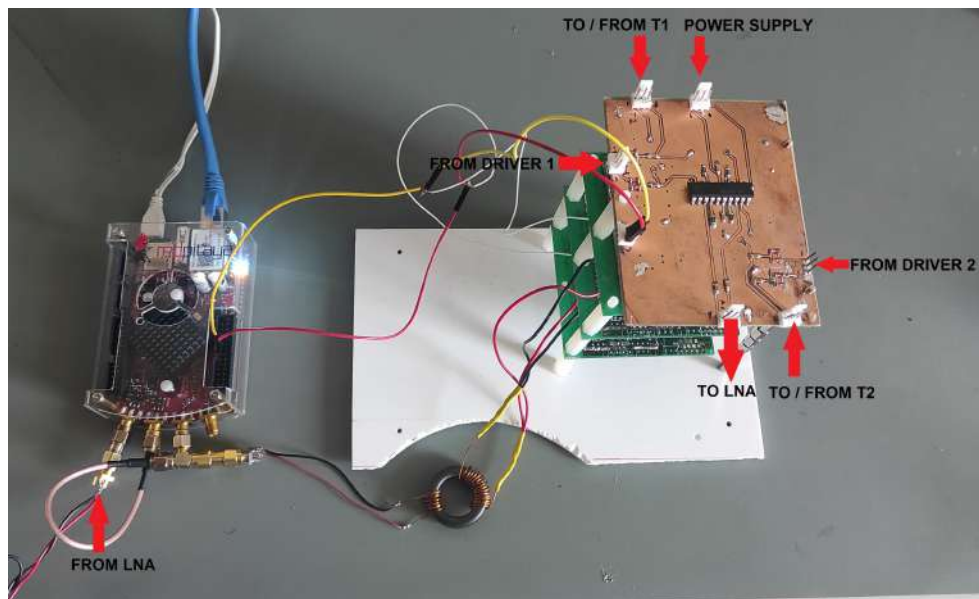


Figure 43: Pin description of the hardware

6. Execute server application:

```
1 ./pulsed-nmr
```

The Makefile and the original C code are also in the folder.

7. In the PC, download a suitable Integrated Development Environment for Python like Spyder.
8. The .csv file with the phase of every pulse will be saved in a folder */stored_data* inside the current directory where the code is being executed. If one desires to change the directory where the phases are stored, change it in line 458.
9. Execute Python application and chose the IP address of the Red Pitaya.

B Appendix: Switch board

B.1 Schematic

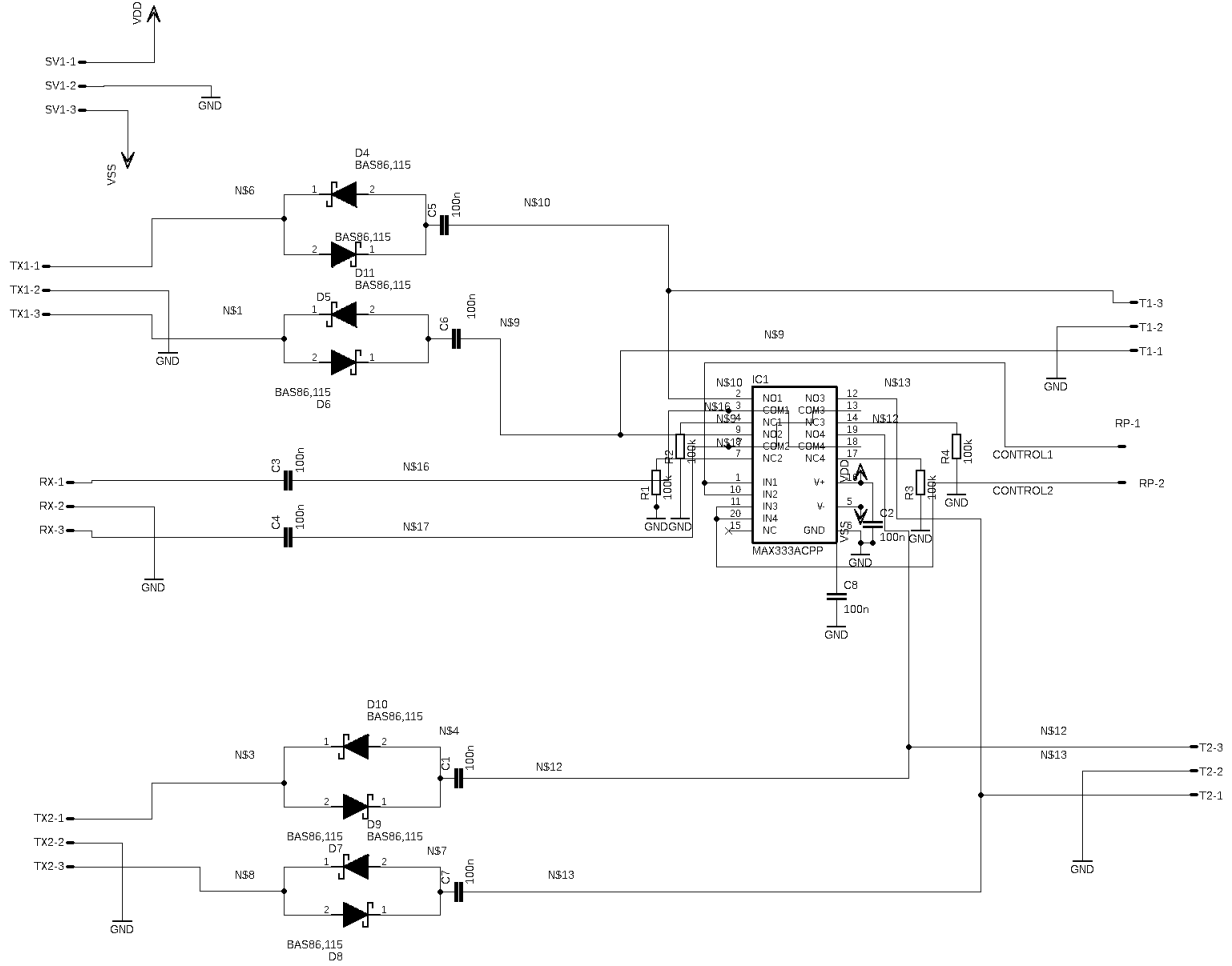


Figure 44: Schematic of analog switch

B.2 PCB layout

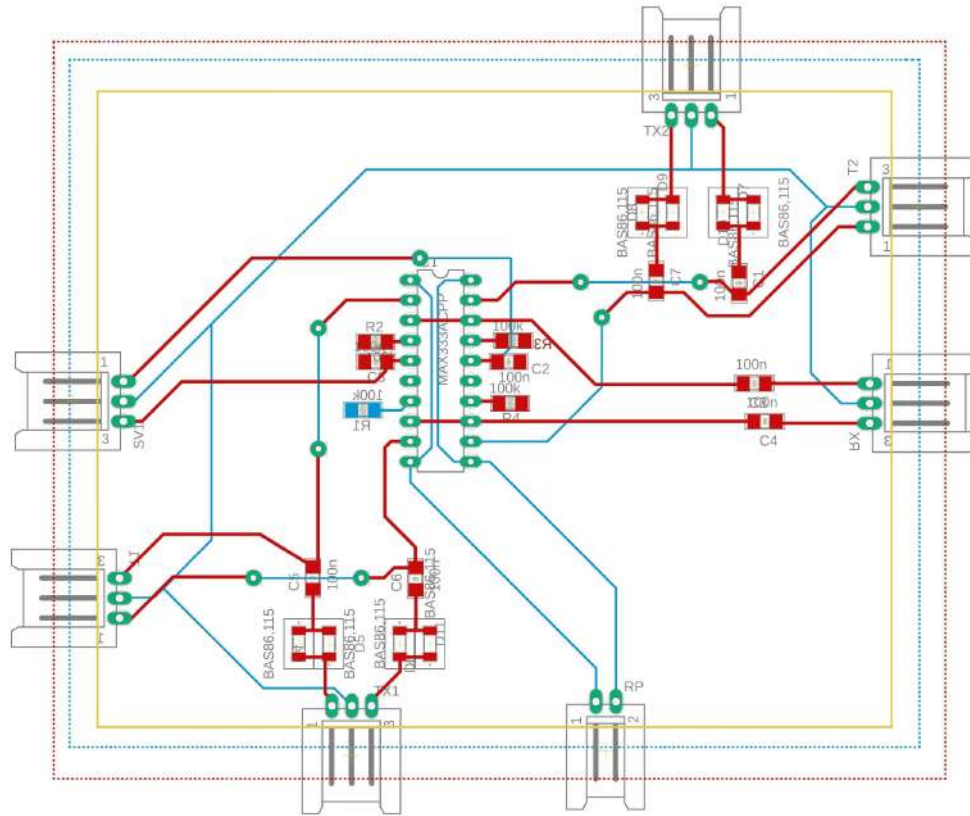


Figure 45: PCB layout of analog switch